Nano Research

ISSN 1998-0124 CN 11-5974/O4
https://doi.org/10.26599/NR.2026.94908838

Ultrasound responsive microneedles for sequential antibacterial and immune regulation in keratitis treatment

Bin Kong[1], Taige Chen[1], Qin Chen[2](✉), Rui Liu[1,2](✉), Tiantian Kong[1](✉), Yuanjin Zhao[2](✉)

[1] School of Biomedical Engineering, Shenzhen University Medical School, Shenzhen University, Shenzhen 518060, China

[2] Department of Rheumatology and Immunology, Nanjing Drum Tower Hospital, School of Biological Science and Medical Engineering, Southeast University, Nanjing 210096, China

Nano Res., **Just Accepted Manuscript** • https://doi.org/10.26599/NR.2026.94908838

https://www.sciopen.com/journal/1998-0124 on May. 13, 2026

© The Authors(s)

Just Accepted

This is a "Just Accepted" manuscript, which has been examined by the peer-review process and has been accepted for publication. A "Just Accepted" manuscript is published online shortly after its acceptance,which is prior to technical editing and formatting and author proofing. Tsinghua University Press (TUP) provides "Just Accepted" as an optional and free service which allows authors to make their results available to the research community as soon as possible after acceptance. After a manuscript has been technically edited and formatted, and the page proofs have been corrected, it will be removed from the "Just Accepted" web site and published officially with volume and article number (e.g., *Nano Research*, **2025**, *18*, 94906990). Please note that technical editing may introduce minor changes to the manuscript text and/or graphics which may affect the content, and all legal disclaimers that apply to the journal pertain. In no event shall TUP be held responsible for errors or consequences arising from the use of any information contained in these "Just Accepted" manuscripts. To cite this anuscript please use its Digital Object Identifier (DOI®),which is identical for all formats of publication.

Just Accepted

TABLE OF CONTENTS (TOC)

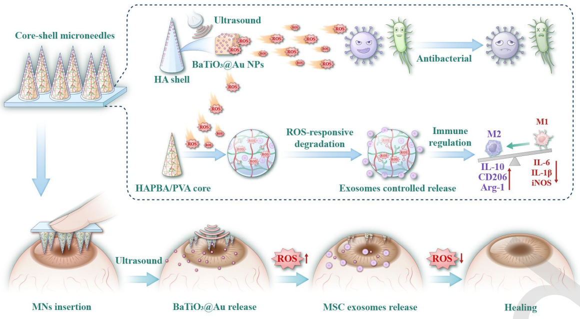

This core-shell microneedle system features a sequential cascade response of antibacterial and immune regulation to promote corneal repair. Initially, the $BaTiO_3$@Au heterostructure enhances piezocatalytic ROS generation under ultrasound, demonstrating potent antibacterial efficacy against both *S. aureus* and *P. aeruginosa*. Subsequently, the ROS-responsive core of the microneedle degrades in the presence of ROS, releasing MSC-derived exosomes, which can effectively scavenge residual ROS, polarize macrophages toward the M2 phenotype, thereby accelerating immune regulation and wound healing.

Nano Research

Open Access

Research Article

Ultrasound responsive microneedles for sequential antibacterial and immune regulation in keratitis treatment

Bin Kong[1], Taige Chen[1], Qin Chen[2] ✉, Rui Liu[1,2] ✉, Tiantian Kong[1] ✉, and Yuanjin Zhao[2] ✉

[1] *School of Biomedical Engineering, Shenzhen University Medical School, Shenzhen University, Shenzhen 518060, China*

[2] *Department of Rheumatology and Immunology, Nanjing Drum Tower Hospital, School of Biological Science and Medical Engineering, Southeast University, Nanjing 210096, China*

Received: 2 February 2026; **Revised:** 12 May 2026; **Accepted:** 13 May 2026

✉Address correspondence to Yuanjin Zhao, yjzhao@seu.edu.cn; Tiantian Kong, ttkong@szu.edu.cn; Rui Liu, liur16_thu@foxmail.com; Qin Chen, chenqin0331@163.com

Cite this article: *Nano Research*, 2026, 19, 94908838 https://doi.org/10.26599/NR.2026.94908838

ABSTRACT: Bacterial keratitis is a leading cause of corneal blindness, yet current antibiotic therapies suffer from poor ocular bioavailability and rising drug resistance. Effective treatment requires not only bacterial eradication but also coordinated anti-inflammation and wound repair. In this paper, we present a “two birds with one stone” strategy for bacterial keratitis treatment based on an ultrasound-activated cascade responsive core-shell microneedle. Upon corneal insertion and ultrasound stimulation, piezoelectric nanoparticles embedded in the MN shell generate reactive oxygen species (ROS) to eliminate bacteria. The elevated ROS levels subsequently trigger the degradation of a ROS-responsive hydrogel core, enabling sustained release of mesenchymal stem cell derived exosomes that neutralize residual oxidative stress, promote macrophage M1 to M2 polarization, and facilitate epithelial barrier restoration. Our proposed formulation demonstrated enhanced therapeutic efficacy in a rat keratitis model, outperforming conventional antibiotic eye drops in bacterial clearance, inflammation resolution, and corneal repair. These findings establish the cascade-responsive core-shell microneedles as a clinically promising strategy for treating bacterial keratitis and other infectious ocular diseases.

KEYWORDS: microneedle; ultrasound; cornea; antibacterial; exosome; ROS

1 Introduction

The cornea serves as a critical determinant of visual acuity [1, 2]. It is located at the outermost layer of the eyeball, making it highly vulnerable to bacterial infections, which can progress to keratitis [3]. Bacterial keratitis can result in corneal perforations and intraocular infections. Without timely and adequate treatment, they can lead to irreversible visual impairment or blindness [4]. Antibiotic eye drops are a standard treatment, while their effectiveness is limited by poor bioavailability due to the unique anatomical features of the cornea. In addition, the misuse of antibiotics can contribute to the emergence of antibiotic-resistant bacterial strains [5]. In contrast, nanoparticles capable of producing reactive oxygen species (ROS) by catalyzing hydrogen peroxide and oxygen under various stimuli have demonstrated efficacy against bacterial infections, with reduced risk of fostering antibiotic resistance [6, 7]. Actually, keratitis in practical treatment requires not only effective bacterial eradication but also anti-inflammation and wound repair, which is crucial for corneal homeostasis and prevention of reinfection [8, 9]. However, strategies that capable of eliminating drug-resistant bacterial infections and cascade responsively, reducing inflammation, and promoting wound healing, have rarely been reported. Thus, there is an urgent need for ocular delivery systems that provide prolonged and effective antimicrobial activity while promoting wound healing for treating bacterial keratitis.

Herein, we present a core-shell microneedles with ultrasound-activated sequential antibacterial, immune regulation, and wound healing ability for keratitis treatment, as illustrated in **Fig. 1**. Sonodynamic therapy (SDT) is a new non-invasive approach that uses ultrasound to activate acoustic sensitizer for generating reactive oxygen species (ROS) [10-13]. Piezoelectric materials, as specific acoustic sensitizers, have shown dramatic progress in various fields because of their ability to convert acoustic mechanical force into an electric field via the piezoelectric effect [14, 15]. This process releases electrons to catalyze substrates and produce ROS, effectively killing cancer cells or bacteria [16, 17]. Additionally, exosomes derived from mesenchymal stem cells (MSCs) can stimulate cells to proliferate and migrate, reduce inflammation, and regulate extracellular matrix deposition and remodeling, thereby enhancing wound healing [18-24]. Despite their potential, the effective and localized delivery of these agents to the ocular surface remains challenging. In contrast, microneedles, widely used for painless, non-invasive, and efficient transdermal drug delivery, offer an alternative solution [25-30]. Their various morphology, such as solid, hollow, porous, core-shell, and pagoda-like structures, confer multifunctionality [31-33]. Although microneedles have been applied for corneal penetration and antibacterial material delivery in keratitis treatment, systems that achieve a cascaded antibacterial and wound healing process using microneedles are rarely reported.

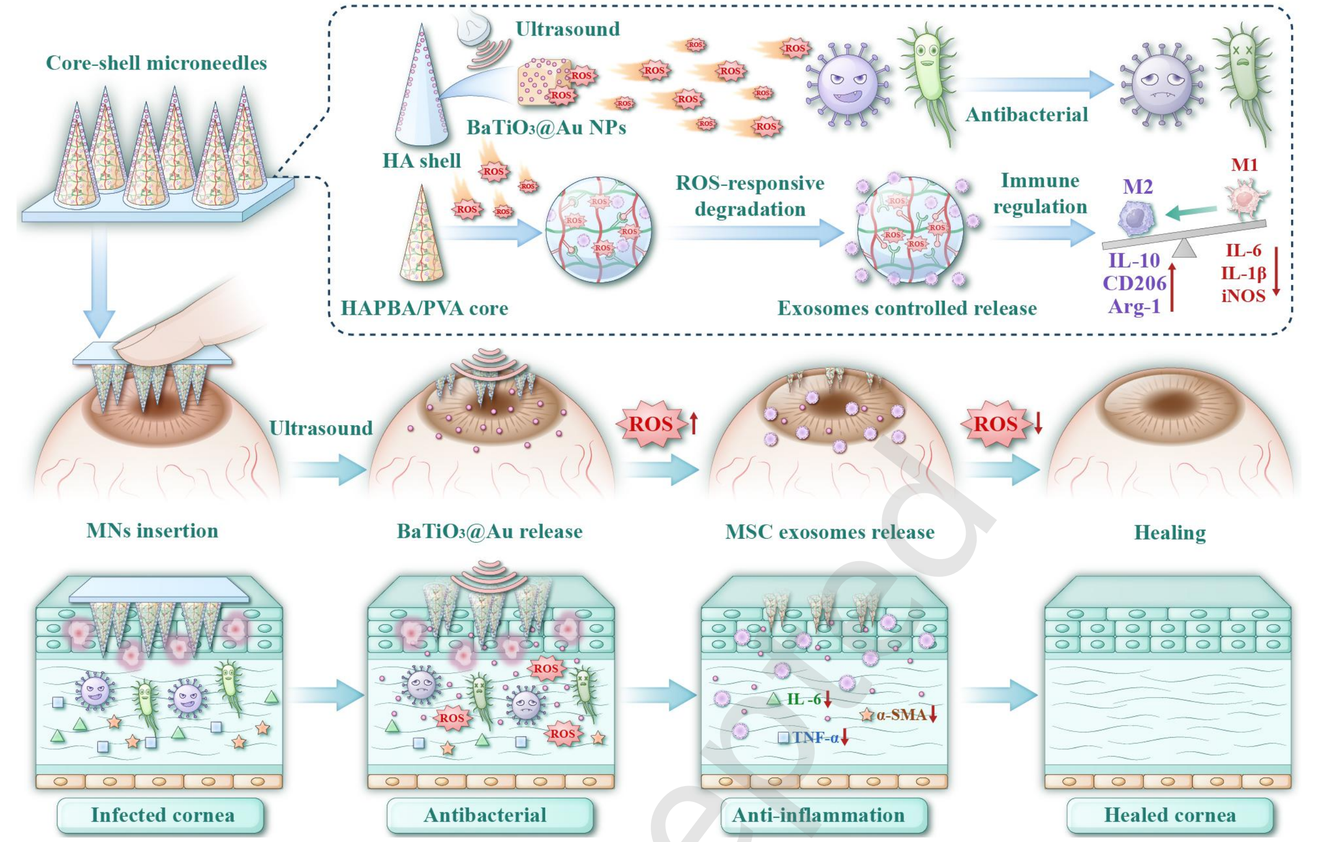

Figure 1 The ultrasound-activated cascade responsive core-shell microneedles for bacterial keratitis treatment.

In this paper, we introduced a "two birds with one stone" strategy for bacterial keratitis treatment based on an ultrasound-activated cascade responsive core-shell microneedle. Biocompatible and soluble hyaluronic acid (HA) was selected as the shell material of the microneedles, incorporating ultrasound responsive gold nanoparticles modified tetragonal barium titanates (BaTiO$_3$@Au) nanoparticles. The core of microneedles consisted of ROS-responsive aminophenylboronic acid-modified HA (HAPBA)/polyvinyl alcohol (PVA) hydrogel, which was used to load MSC-derived exosomes. Upon penetration into the cornea, the HA shell dissolved rapidly, releasing BaTiO$_3$@Au nanoparticles. Under ultrasound irradiation, BaTiO$_3$@Au catalyzed the surrounding oxygen and water, generating ROS to eliminate bacteria. Subsequently, the HAPBA/PVA core degraded gradually in the presence of ROS, facilitating a sustained release of exosomes. This process enhanced the proliferation and migration of corneal epithelial cells while neutralizing residual ROS. Additionally, exosomes could regulate macrophage activity, reduce inflammation, and promote repair. Thus, the designed microneedle demonstrated enhanced therapeutic efficacy in a rat keratitis model infected by Staphylococcus aureus. Unlike conventional microneedle systems that rely on pre-programmed passive release, our design uniquely exploits the piezocatalytically generated ROS as both the bactericidal agent and the endogenous trigger that activates reparative exosome release, forming a self-adaptive, single trigger cascade that directly couples antibacterial action to immune regulated repair. These findings demonstrate that the cascade-responsive microneedles represent an improvement over existing therapeutic modalities, establishing them as promising candidate for combating diverse bacterial infections.

2 Results and discussion

HA has good biocompatibility and biodegradability, which has demonstrated therapeutic potential in various ophthalmology diseases [34, 35]. For instance, within the realm of dry eye management, HA is a prevalent component of artificial tears, functioning primarily as an ocular lubricant [36]. Therefore, HA based biomaterials were chosen as the main component of our microneedle system. In a typical experiment, HAPBA was synthesized through linking 3-(aminomethyl) phenylboronic acid (PBA) to the polysaccharide backbone of HA, as shown in **Fig. S1(a)**. ^{1}H NMR and FTIR analyses confirmed the attachment of PBA to the HA polymer (**Fig. S1(b, c)**). The ^{1}H NMR spectrum exhibited characteristic peaks for the PBA benzene rings (7.0-8.0 ppm, marked with b, c, d, e) and HA methyl groups (2.0 ppm, marked with a). FTIR data further supported this: C=O vibration of HA's carboxyl appeared at 1604 cm^{-1}, while new absorptions at 1561 cm^{-1} (C=O vibration of –CONH–) and 1372 cm^{-1} (B-O from PBA) emerged in the HAPBA spectrum. After grafting with the PBA moiety, HA would crosslink with 1,3-diol groups on PVA to form hydrogels through boronic ester linkages [37, 38].

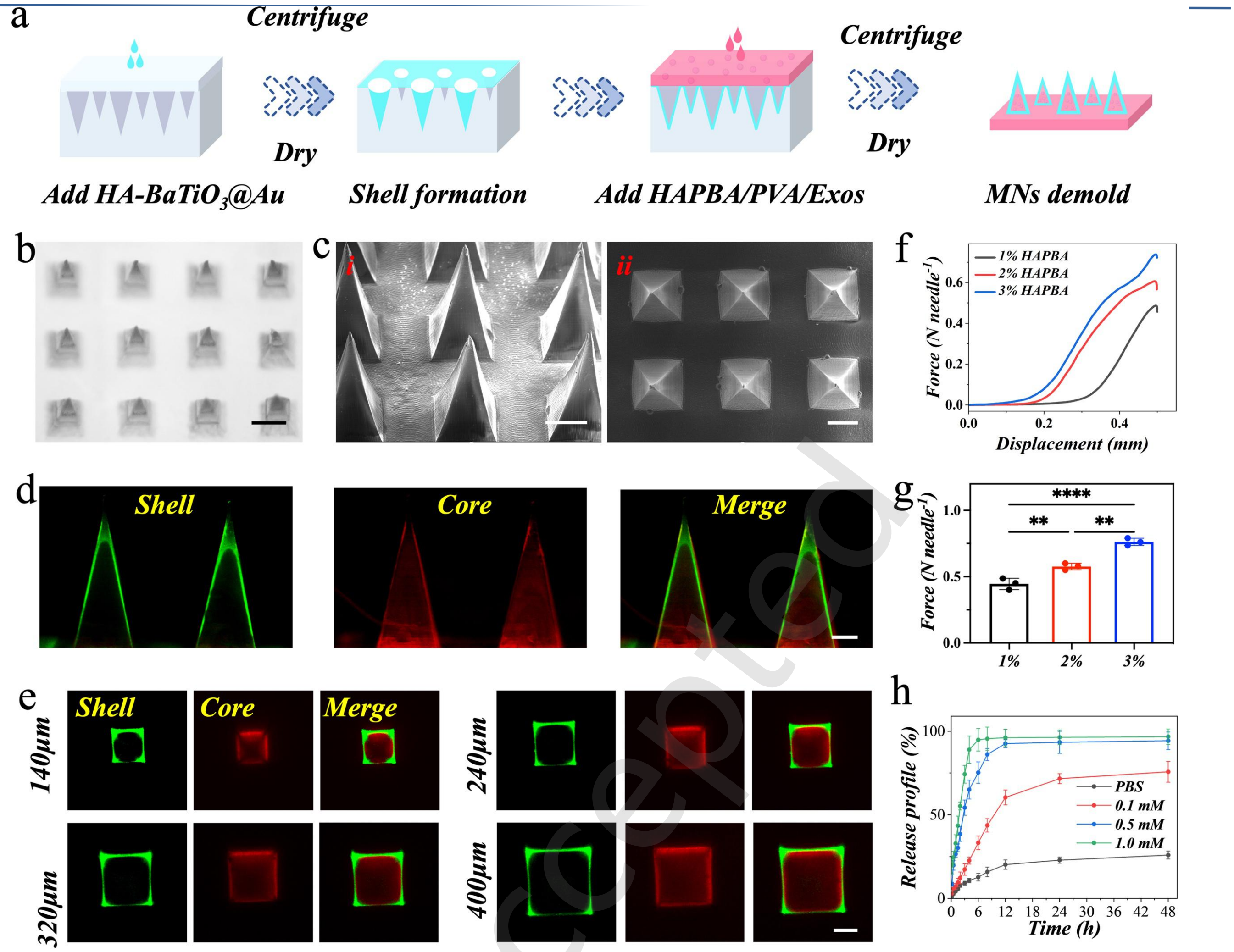

Figure 2 Fabrication and Characterization of the core-shell microneedles. (a) The scheme showing the preparation of core-shell microneedles. The Photograph (b) and SEM images (c) of the microneedles. (d) Fluorescent images show the core-shell structure of the microneedles. (e) Fluorescent images show the cross-section structure of the microneedles under different height. Force-displacement curve (f) and maximum force data (g) of the microneedles composed of different concentrations of HAPBA. n=3, biologically independent samples. Data are showed as mean ± SD. **P < 0.01; ****P < 0.0001, using one-way ANOVA followed by post-hoc test. (h) Releasing profiles of FITC-BSA incorporated microneedles under different concentrations of H_2O_2. n=3, biologically independent samples. Data are showed as mean ± SD. Scale bars: 300 μm in (b), 200 μm (c), 100 μm in (d) and (e).

After the successful synthesis of HAPBA, responsive core-shell microneedles were prepared by a simple template replication method [39-41]. In brief, the HA solution was centrifuged into the microcavities of a polydimethylsiloxane (PDMS) mold. Following overnight ambient drying, hollow microneedle structure could form due to the preferential adhesion of the hydrophilic and viscous HA polymer to the plasma-treated, hydrophilic PDMS cavity surfaces. Subsequently, the residual cavities were filled with the pregel solution of HAPBA and PVA under a vacuum. To fabricate the supporting substrate, pure PVA solution was applied on the mold and dried. Finally, the completed core-shell microneedle was demolded and successfully fabricated. From the optical and scanning electron microscopy (SEM) images, microneedle with a 10 × 10 array had a square pyramid shape, with a height of 500 μm and a base diameter of 320 μm (**Fig. 2(a-c)**). To further verify the core-shell structure of the microneedle, two types of fluorescent dye, including FITC-bovine serum albumin (BSA) and rhodamine B (rhB) were loaded into the shell and core layer of the microneedle. From **Fig. 2(d, e)**, red rhB and green BSA can be separately encapsulated in the inner and outer layers of microneedle, respectively, confirming the core-shell structure of the microneedle.

Adequate mechanical strength is critical for successful tissue penetration by microneedles [42-44]. Consequently, the compressive force of microneedles was quantified using a mechanical testing apparatus (**Fig. 2(f, g)**). We measured and comparatively assessed the microneedles prepared from HAPBA solutions at concentrations of 1%, 2%, and 3%. The results demonstrated that increasing polymer concentration yielded greater compressive force. Notably, the maximum compressive force exhibited by 1% HAPBA (0.45 ± 0.04 N) exceeded the threshold required for penetrating corneal tissue [45]. In addition, rat corneas were utilized to evaluate the microneedle penetration capability and safety via insertion. HE staining was performed to examine corneal morphology before and after MN application. As evidenced in **Fig. S2**, MNs readily penetrated the epithelial layer. To further verify corneal penetration, rhodamine B-loaded microneedles were inserted into rat corneas and the tissue was imaged by confocal microscopy after needle removal. A sharp fluorescent track extending from the epithelial surface to approximately 120 μm depth was observed, matching the tapered geometry of the MN tip (**Fig. S3**). Furthermore, the impact of microneedle insertion on corneal cell viability was assessed via immunofluorescent staining for apoptosis using the TUNEL assay. As demonstrated in **Fig. S2**, MN application induced no significant apoptosis in corneal cells.

Boronic ester-based hydrogel networks exhibit sensitivity to low pH, elevated glucose, and ROS, which can lead to potential structural disruption, facilitating the controlled release of encapsulated bioactive materials [46-48]. To verify the ROS-responsibility of our microneedles with the core of HAPBA/PVA hydrogel, we encapsulated FITC-BSA within the core and immerse the microneedles in PBS solution with H_2O_2. As shown in **Fig. 2(h)**, BSA release from the microneedles in pure PBS exhibited slower kinetics, achieving only 20.2±2.8% cumulative release after 12 hours. However, incubation in 0.1 mM H_2O_2 substantially accelerated BSA release, yielding 60.4 ± 4.4% cumulative release within the same time, indicative of high H_2O_2 sensitivity. Besides, progressive acceleration of BSA release was observed with increasing H_2O_2 concentrations. In addition, in the ex vivo infected cornea model, US application triggered an immediate ROS burst, with fluorescence peaking at 45000 a.u. at 0 h and declining rapidly thereafter. In contrast, exosome concentration rose from a baseline of 5 μg/mL at 0 h to a maximum of 21.0 μg/mL at 2 h, clearly lagging behind the ROS peak. This time-staggered profile provides direct evidence for the sequential cascade (**Fig. S4**).

To realize the cascade responsive ability of the microneedle system, $BaTiO_3$ was selected to be incorporated within the HA shell. As a classical piezoelectric material, $BaTiO_3$ finds extensive application in biosensing, piezocatalysis, and biomedicine. Metal-piezoelectric heterostructures can establish Schottky barriers, enhancing catalytic performance by facilitating ROS generation through interactions between piezoelectric charges and ambient H_2O and O_2. To leverage this effect, gold nanoparticles were deposited on $BaTiO_3$ nanocubes to construct heterostructures (**Fig. 3(a)**). The Au NPs were deposited onto $BaTiO_3$ nanocubes via an in-situ chemical reduction process, where Au^{3+} ions are reduced by $NH_3 \cdot H_2O$ to metallic Au^0 that nucleates directly on the $BaTiO_3$ surface, forming chemisorptive Au-O-Ti interfacial bonds rather than simple physical attachment. This process forms chemisorptive Au-O-Ti interfacial bonds rather than simple physical attachment, and the work function mismatch between Au (~5.1 eV) and $BaTiO_3$ (~4.2 eV) drives the formation of a Schottky barrier at the metal-semiconductor interface, which suppresses electron-hole recombination and enhances piezocatalytic ROS generation under ultrasound.

Electron microscopy analysis confirmed successful Au NP decoration, with SEM and transmission electron microscopy (TEM) images (**Fig.s 3(b, c)**) revealing randomly dispersed Au NPs on cubic $BaTiO_3$ surfaces. Elemental mapping further confirmed Au NP distribution across $BaTiO_3$ nanocubes (**Fig. S5**). X-ray photoelectron spectroscopy (XPS) elucidated surface compositions and oxidation states, with survey spectra indicating Bi, O, Ti, Au, and C presence (**Fig. S6(a)**). High-resolution Au 4f spectra (**Fig. 3(d)**) exhibited characteristic peaks at 83 eV (Au $4f_{7/2}$) and 87 eV (Au $4f_{5/2}$). A redshift in UV-vis absorption relative to pristine $BaTiO_3$ (**Fig. S6(b)**) provided additional evidence of heterostructure formation. Hydrodynamic diameter analysis indicated an increase from 139.3±2.8 nm ($BaTiO_3$) to 150.6±8.6 nm ($BaTiO_3$@Au), consistent with surface-bound Au NPs. Zeta potential measurements demonstrated a reduction from -26.4±1 mV ($BaTiO_3$) to -31.4±3.3 mV ($BaTiO_3$@Au), attributable to the inherent negative surface charge of Au NPs (**Fig. S7**). All the results demonstrated that $BaTiO_3$@Au NPs were prepared successfully.

The piezocatalytic capacities of $BaTiO_3$@Au for producing ROS under US irradiation were investigated based on electron spin resonance (ESR) spectroscopy to detect hydroxyl radical (·OH) and singlet oxygen ($^1O_2$). Characteristic signatures were observed: the 1:2:2:1 quartet for DMPO (·OH adducts, **Fig. 3(e)**) and the 1:1:1 triplet for TEMP ($^1O_2$ adduct, **Fig. 3(f)**). Quantitative analysis revealed a 3-fold enhancement in ·OH signal intensity for $BaTiO_3$@Au+US versus $BaTiO_3$+US, and a 16-fold increase versus US alone. A similar enhancement trend was observed for $^1O_2$ generation. Control experiments confirmed negligible ROS signals from $BaTiO_3$@Au nanocomposites without US excitation. These data demonstrate that the Schottky junction markedly amplifies the sonodynamic efficacy of piezoelectric nanomaterials, substantially increasing ROS yield. Critically, US irradiation acts through cavitation effects and is essential for initiating the piezotronic effect. This mechanism reduces the interfacial energy barrier at the Au-$BaTiO_3$ junction, facilitating electron transfer from Au to $BaTiO_3$ and suppressing electron-hole recombination. The transferred electrons subsequently generate cytotoxic ·OH and $^1O_2$.

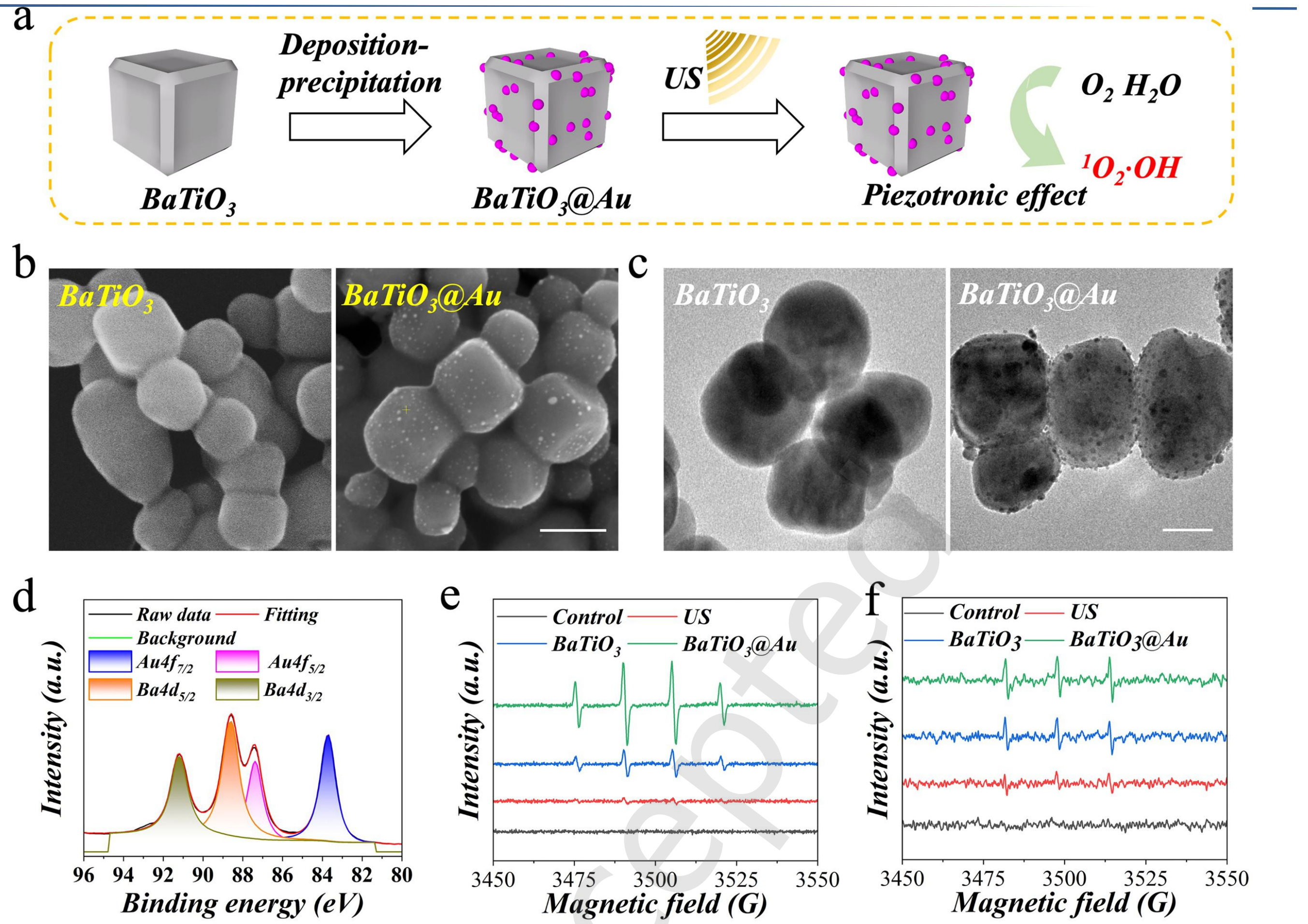

Figure 3 Synthesis of BaTiO3@Au NPs and US triggered ROS production. (a) Schematic illustrating the preparation of BaTiO$_3$@Au NPs and their abilities to generate ROS under US. (b) SEM and (c) TEM micrographs of the BaTiO$_3$ and BaTiO$_3$@Au. (d) XPS spectra. ESR measurement for the detection of (e) ·OH and (f) ^{1}O$_2$. Scale bars: 100 nm in (b), 50 nm in (c).

Following the preparation of BaTiO$_3$@Au nanoparticles, US responsive microneedle was fabricated via integrating the nanocomposites within a HA shell. To assess biocompatibility and therapeutic potential, Live/Dead viability assays were performed on human corneal epithelial cells (HCECs) and human keratocytes (HKs). Cells were cultured in transwell systems for 72 hours with microneedles containing BaTiO$_3$@Au at concentrations of 0, 50, 100, and 200 μg/mL. **Fig. S8-S9** demonstrated negligible reduction in cellular viability across all experimental groups, confirming excellent cytocompatibility of the engineered microneedles. Besides, *in vivo* fluorescence imaging revealed that BaTiO$_3$@Au nanoparticles injected into the corneal stroma were gradually cleared over time: a strong signal at day 0 progressively weakened by day 3, and only minimal residual fluorescence remained at day 7 (**Fig. S10**). Furthermore, long-term histological and immunohistochemical analyses one month post-injection demonstrated intact corneal architecture, normal collagen organization, and negligible IL-6 or TNF-α upregulation, indistinguishable from untreated controls (**Fig. S11**). These results collectively indicate that the nanoparticles are efficiently eliminated from the cornea without inducing chronic inflammation or fibrosis.

The antibacterial efficacy of US activated microneedles was evaluated against *Staphylococcus aureus* (*S. aureus*) and *Pseudomonas aeruginosa* (*P. aeruginosa*) (**Fig. 4(a)**). Bacterial suspensions were incubated for 1 h with MNs, MNs+BaTiO$_3$, and MNs+BaTiO$_3$@Au for 1 h followed by 5-min US exposure. Untreated bacteria served as controls. Colony-forming unit (CFU) assays revealed minimal bactericidal activity in the MNs+US group versus controls, indicating negligible intrinsic antibacterial effects from materials or ultrasound alone. Significant bacterial reduction occurred in BaTiO$_3$-containing groups under US stimulation, with BaTiO$_3$@Au+US exhibiting maximal efficacy (**Fig. 4(b)**).

Complementary to CFU assays, bacterial viability was quantitatively assessed via staining of SYTO 9 and PI (**Fig. 4(c)**). Treatment groups exhibited dose-dependent viability reduction in both species. As shown in **Fig. 4(d)**, *S. aureus* viability declined from 83.1±5.1% (control) to 75.2±4.2% (MNs+US), 49.7±5.4% (MNs+BaTiO$_3$+US), and 13.3±6.2% (MNs+BaTiO$_3$@Au+US). From **Fig. 4(e)**, *P. aeruginosa* viability decreased from 93.9±6.7% (control) to 84.8±2.6% (MNs+US), 41.3±5.4% (MNs+BaTiO$_3$+US), and 7.7±3.3% (MNs+BaTiO$_3$@Au+US). SEM results corroborated these findings, showing pronounced membrane disruption in bacteria treated with MNs+BaTiO3@Au+US. The severity of this morphological compromise correlated directly with treatment efficacy (**Fig. 4(f)**).

To further assess efficacy against drug-resistant bacteria, we challenged the microneedle system with methicillin-resistant Staphylococcus aureus (MRSA). The MNs+BaTiO$_3$@Au+US treatment reduced bacterial survival to 15%, markedly outperforming the commercial tobramycin eye drop (32% survival). This advantage confirms that the ROS-based piezocatalytic mechanism physically disrupts bacteria independent of conventional resistance pathways, providing a robust strategy against drug-resistant keratitis (**Fig. S12**).

Collectively, these data demonstrated that US activates $BaTiO_3$-mediated ROS generation for bacterial eradication, while gold functionalization potentiates this effect through enhanced piezocatalytic activity.

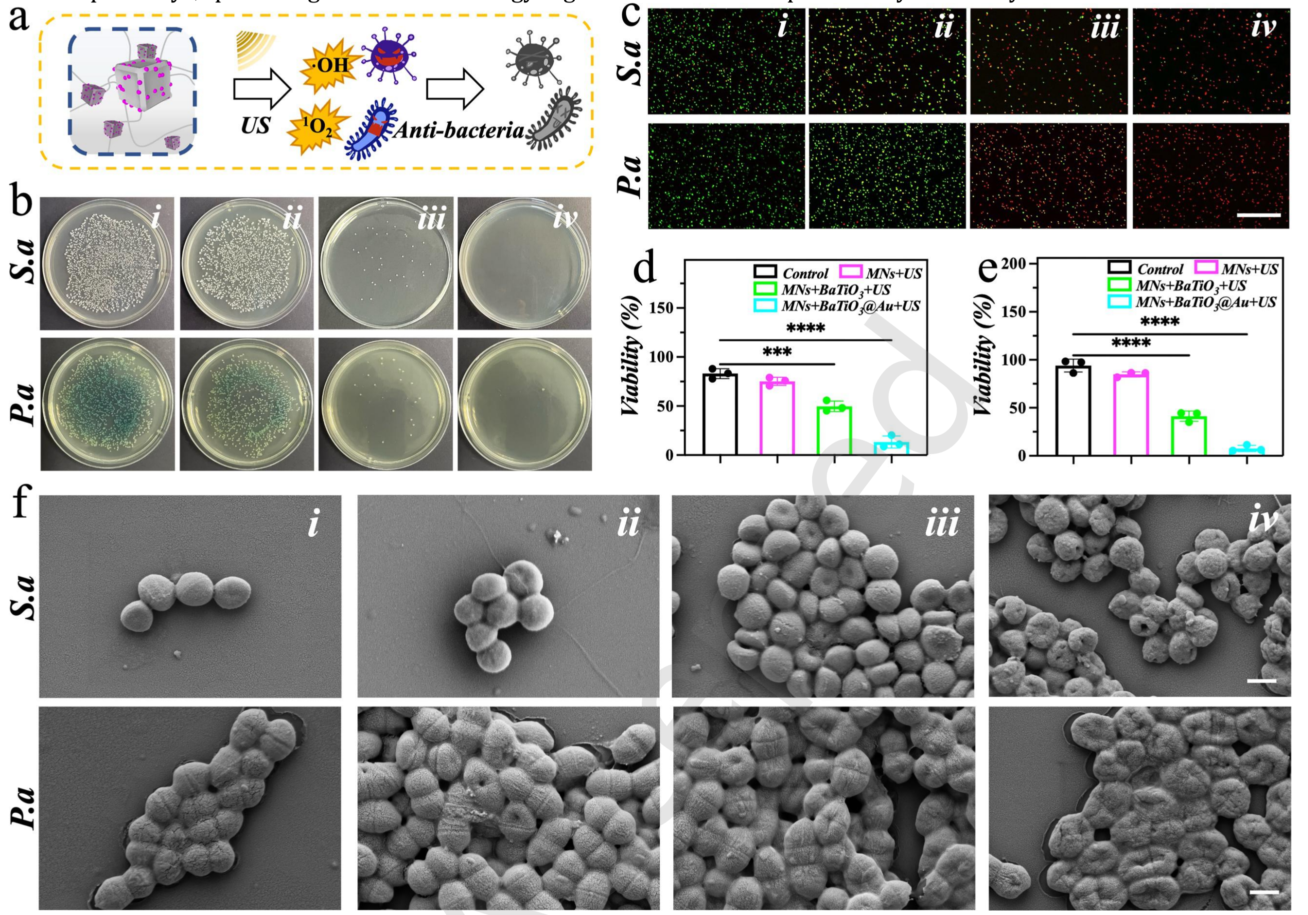

Figure 4 In vitro antimicrobial efficacy of $BaTiO_3$@Au loaded microneedles. (a) Schematic representation of the antibacterial mechanism. (b) Bacterial colony formation on agar plate following therapeutic interventions: (i) buffer control, (ii) MNs+US, (iii) MNs+$BaTiO_3$+US, and (iv) MNs+$BaTiO_3$@Au+US. (c) Fluorescence micrographs visualizing bacterial viability under corresponding treatment conditions. Quantitative viability assessment of (d) *S. aureus* and (e) *P. aeruginosa*. n=3, biologically independent samples. Data are showed as mean ± SD. ***P < 0.001; ****P < 0.0001, using one-way ANOVA followed by post-hoc test. (f) Bacteria SEM images after treatment. Scale bars: 50 μm in (c); 500 nm in (f).

Exosomes derived from MSCs have shown potential to stimulate cell proliferation and migration, reduce inflammation, and regulate extracellular matrix deposition and remodeling, thereby enhancing wound healing [20]. Thus, we incorporated exosomes within the ROS-responsive HAPBA/PVA core of the microneedle to achieve the cascade antibacterial and wound healing (**Fig. 5(a)**). Transmission electron microscopy confirmed typical cup-shaped morphology of exosomes (**Fig. S13(a)**), while nanoparticle tracking analysis revealed a monodisperse size distribution (132 nm) consistent with exosomal parameters (**Fig. S13(b)**) [49]. We further validated exosomes through characteristic biomarkers: positive for CD 63, CD 9, and TSG 101 (**Fig. S13(c)**). To assess the capacity of HCECs to internalize exosomes, DiD-labeled exosomes were co-cultured with the cells for 2 and 12 hours. Fluorescent images demonstrated successful uptake of exosomes into HCECs. Furthermore, exosomal internalization exhibited a time-dependent increase, with higher levels observed at the 12-hour time point compared to 2 hours (**Fig. S14**).

The cytoprotective capacity of exosomes against oxidative stress was evaluated in HCECs using DCFH-DA fluorescence. The fluorescent staining results indicated that H_2O_2 stimulation (250 μM) significantly elevated intracellular ROS, while co-treatment with exosomes dose-dependently attenuated this response. Flow cytometric quantification confirmed concentration-dependent antioxidant efficacy, showing progressive reduction in fluorescence intensity (**Fig. S15**). Additionally, the effect of exosomes on the wound healing was evaluated using scratch assays of HCECs. Compared to the MNs group, the MNs+Exo treatment demonstrated enhancement in the scratch wound closure rate (**Fig. S16**).

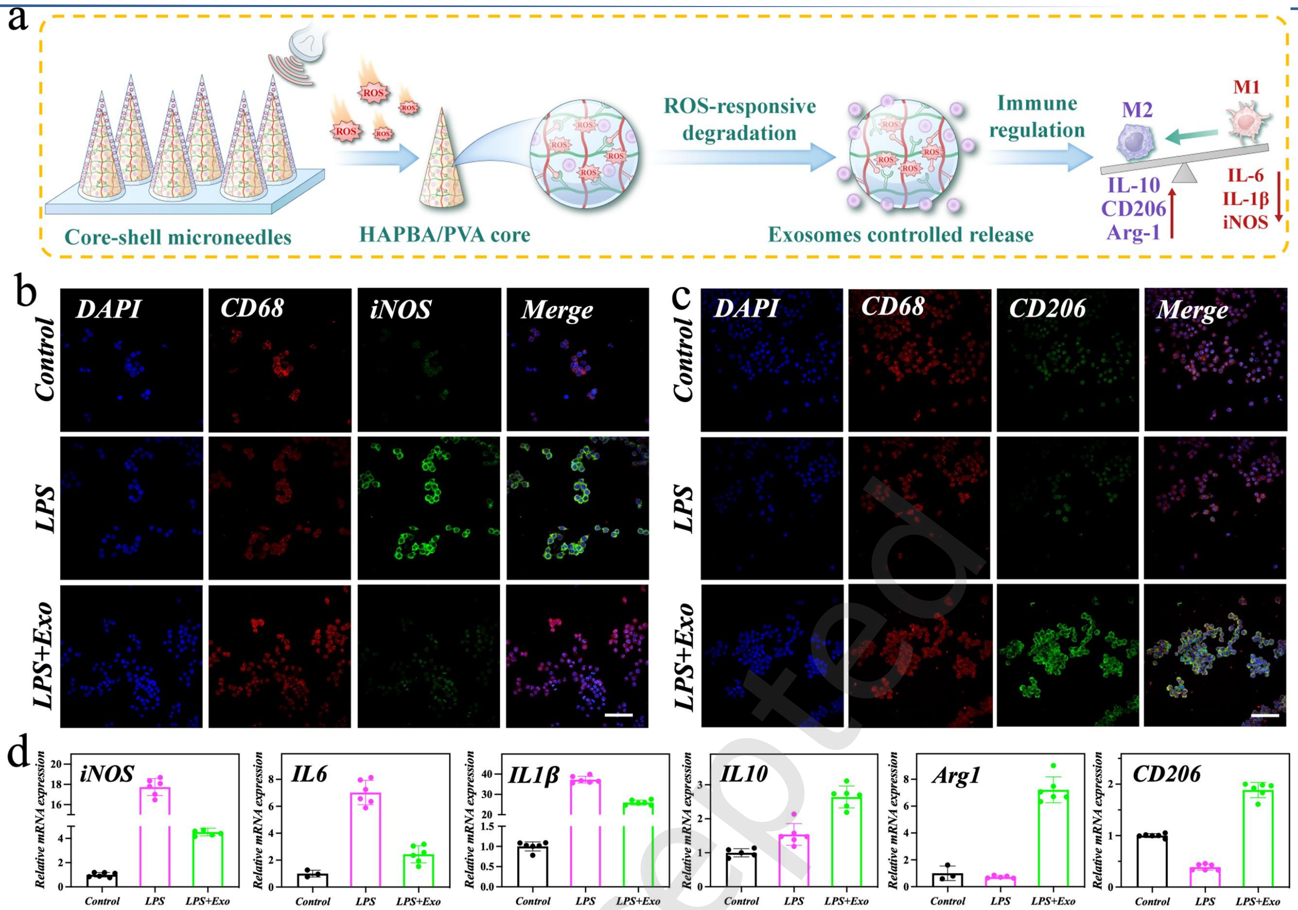

Figure 5 In vitro immunomodulatory effects of the microneedles. (a) Schematic diagram. Representative immunofluorescence images for CD 68 (red), iNOS (green, b) and CD 206 (green, c) in Raw264.7 cells after different treatment. (d) Expression of M1 and M2 related genes in Raw264.7 cells after different treatment. Scale bars: 50 µm.

In addition, we performed experiments to evaluate the validation of exosome stability after microneedle encapsulation and ultrasound/ROS exposure. TEM and NTA analyses confirmed that exosomes retained their characteristic cup-shaped morphology and monodisperse size distribution after microneedle encapsulation and ultrasound/ROS exposure, with no signs of aggregation or membrane disruption (**Fig. S17(a, b)**). Functionally, exosomes from all conditions exhibited comparable ROS-scavenging capacity in H2O2-challenged HCECs, as quantified by DCFH-DA fluorescence (**Fig. S17(c)**). These results collectively verify that the therapeutic functionality of MSC exosomes is fully preserved during fabrication and throughout the US-triggered cascade release process.

Macrophages critically regulate immune defense and wound repair through inflammatory cytokine secretion [50-53]. Classically activated (M1) macrophages release pro-inflammatory mediators to initiate inflammation, whereas alternatively activated (M2) macrophages release anti-inflammatory mediators, suppressing T cell responses and facilitating tissue regeneration [54, 55]. Thus, we employed LPS-stimulated RAW264.7 macrophages to assess the comparative anti-inflammatory efficacy of exosomes. Immunofluorescent images demonstrated that LPS induction elevated iNOS (M1 marker) and suppressed CD206 (M2 marker) expression. Treatments progressively attenuated iNOS while augmenting CD206 signals, indicating a shift from M1 towards M2 polarization (**Fig. 5(b, c)**). Besides, M1 and M2 associated macrophage gene expression profile was determined by qPCR. The results revealed that exosomes significantly induced M2 related genes while suppressing M1 related markers (**Fig. 5(d)**). Collectively, the synergistic ROS scavenging and immunomodulatory abilities endowed exosomes with the potential to improve wound healing.

Building on promising in vitro antibacterial and wound healing properties, $BaTiO_3$@Au and exosome loaded core-shell microneedles were evaluated in a S. aureus induced rat keratitis model (**Fig. 6(a)**). *In vivo* biocompatibility was assessed by subcutaneous implantation, with hematoxylin&eosin (HE) stained primary tissues revealing no significant histopathological differences versus native tissues (**Fig. S18**). *In vivo* corneal confocal microscopy demonstrated that the endothelial cell monolayer remained intact and regularly arranged after either ultrasound alone (US, $1.5\ W/cm^2$, 5 min) or combined MNs+$BaTiO_3$@Au+US treatment. These findings confirm that the ultrasound parameters employed are safe for both the anterior segment and systemic tissues (**Fig. S19**).

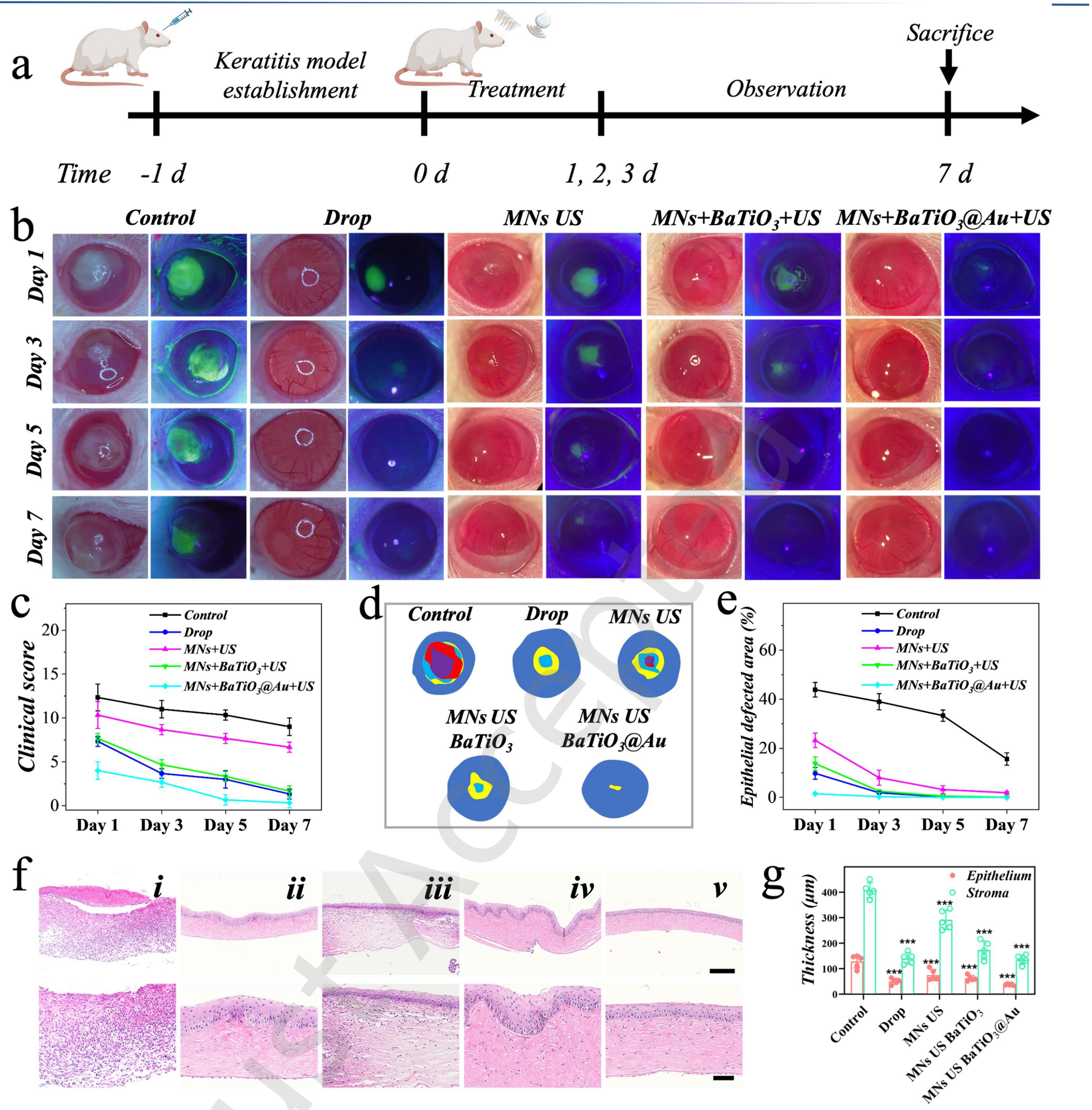

Figure 6 Antibacterial verification of the core-shell microneedles in vivo. (a) Schematic of S. aureus-induced keratitis model and therapeutic regimen. (b) Representative photographs (left) and fluorescein sodium staining images (right) from Day 1 to 7 in control (untreated), Drop, MNs+US, MNs+BaTiO$_3$+US, and MNs+BaTiO$_3$@Au+US groups. (c) Clinical scores. n=5, biologically independent samples. Data are showed as mean ± SD. (d) Graphic expression shows the variation of the wound area with time. (e) Quantification of epithelial defects from (b). n=5, biologically independent samples. Data are showed as mean ± SD. (f) HE stained cornea sections at day 7. (g) Thickness quantification of epithelium and stroma in infected corneas at day 7. n=5, biologically independent samples. Data are showed as mean ± SD. ***P < 0.001, using one-way ANOVA followed by post-hoc test. Scale bars: 200 μm in (f), 50 μm in the enlarged images.

aureus infected rats were divided into untreated control, tobramycin/dexamethasone eye drops (Drop), MNs+US, MNs+BaTiO$_3$+US, and MNs+BaTiO$_3$@Au+US groups. Representative corneal photographs at days 1, 3, 5, and 7 post-treatments documented two parameters: corneal opacity (left panels) and fluorescein sodium staining, which could quantify the epithelial defects (right panels) (**Fig. 6(b)**). Severe infection persisted in control and MNs+US groups, exhibiting marked opacity and visible defects throughout the study. The Drop group showed moderate improvement, with reduced epithelial defect area and delayed opacification compared to the untreated control and MNs+US group. Although partial wound resolution occurred by day 7, these groups remained in the inflammatory phase with persistent clouding. The MNs+BaTiO$_3$@Au+US group demonstrated optimal therapeutic outcomes, significantly delaying corneal opacification and defect expansion while suppressing inflammation (**Fig. 6(c-e)**). Corneas treated with MNs+BaTiO$_3$@Au+US exhibited negligible bacterial colonies on agar plates, representing an obvious reduction compared to both the untreated control and the MNs+US group, and notably outperforming the commercial antibiotic eye drop group. This result provides direct microbiological evidence that the piezocatalytically generated ROS reaches therapeutically adequate levels within the authentic infected cornea (**Fig. S20**).

HE analysis of day 7 corneal sections revealed near-normal epithelial/stromal thickness in both $BaTiO_3$-containing treatment groups versus controls (**Fig. 6(f, g)**). Substantial inflammatory infiltrates characterized control and MNs+US groups, whereas MNs+$BaTiO_3$+US and MNs+$BaTiO_3$@Au+US groups showed minimal infiltration. Collagen immunofluorescence (**Fig. S21**) indicated elevated collagen deposition in $BaTiO_3$-treated groups, with MNs+$BaTiO_3$@Au+US exhibiting optimally aligned fibers, suggesting advanced tissue remodeling.

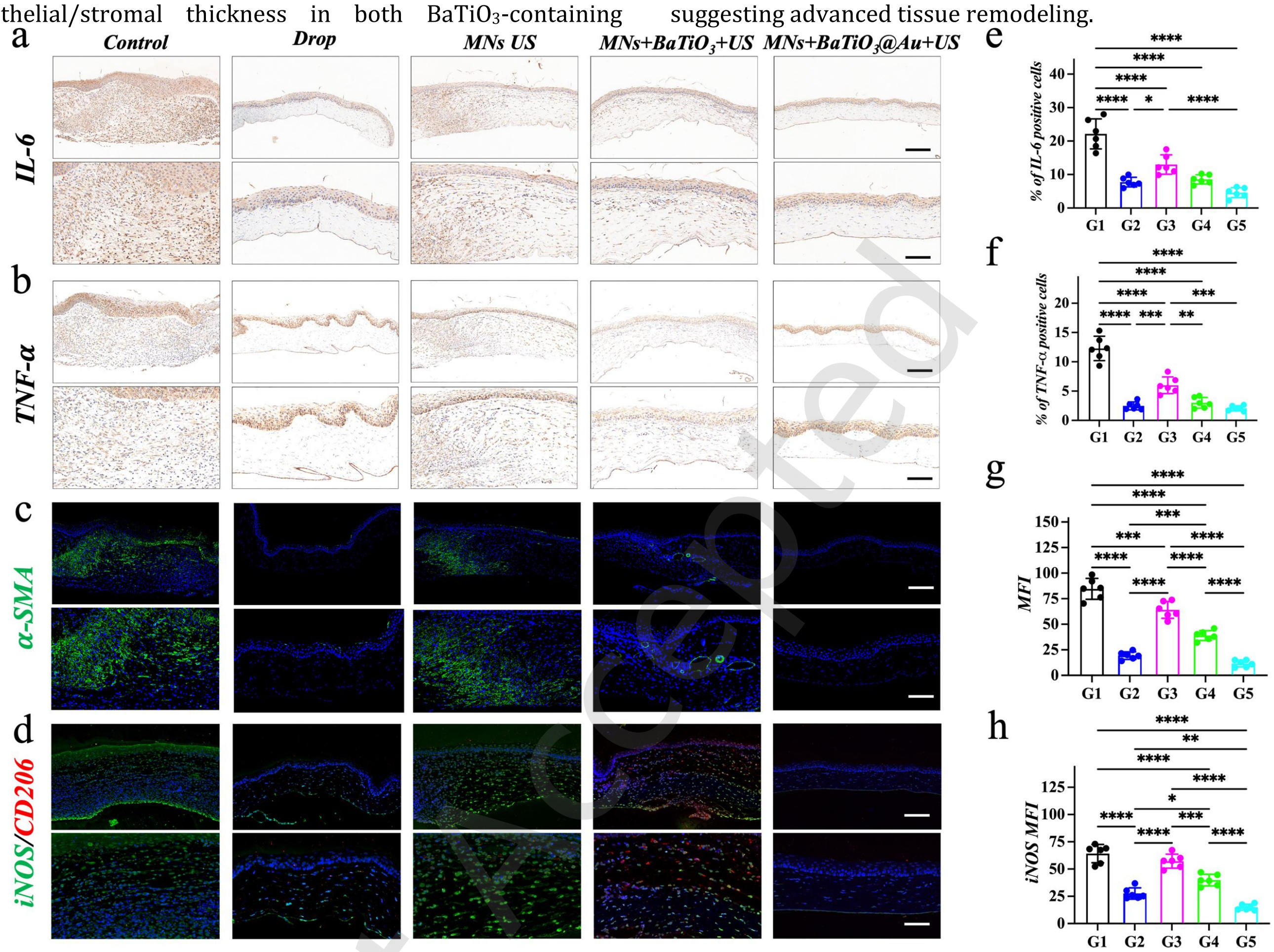

Figure 7 Immunological antibacterial, anti-inflammation, and prohealing evaluation of the core-shell microneedles. Representative immunohistochemistry staining images of IL-6 (a) and TNF-α (b), immunofluorescent staining images of α-SMA (c) and iNOS/CD 206 (d) representative histopathological sections of infected cornea subjected to: untreated cornea (G1), Drop (G2), MNs+US (G3), MNs+$BaTiO_3$+US (G4), and MNs+$BaTiO_3$@Au+US (G5). (e) Quantification of IL-6 positive cells in (a). (f) Enumeration of TNF-α cells in panel (b). (g) Mean fluorescence intensity of α-SMA in (c). (h) Mean fluorescence intensity of iNOS in (d). n=6, biologically independent samples. Data are showed as mean ± SD. $*P < 0.05$; $**P < 0.01$; $***P < 0.001$; $****P < 0.0001$, using one-way ANOVA followed by post-hoc test. Scale bars: 200 μm. 100 μm in the enlarged images.

Immunohistochemical/immunofluorescent evaluation of inflammatory mediators (IL-6, TNF-α), angiogenesis marker α-SMA, and macrophage-specific marker iNOS/CD206 further validated treatment efficacy (**Fig. 7(a-d)**). Quantification confirmed reduced IL-6/TNF-α cells in $BaTiO_3$-treated groups versus controls (**Fig. 7(e, f)**). The Drop group demonstrated a partial reduction in IL-6 and TNF-α expression relative to the MNs+$BaTiO_3$+US, but the levels remained higher than those in the MNs+$BaTiO_3$@Au+US group. The MNs+$BaTiO_3$@Au+US group showed significantly attenuated α-SMA fluorescence intensity (**Fig. 7(g)**). ZO-1 immunofluorescence demonstrated progressive restoration of the corneal epithelial tight junction barrier from the untreated control and MNs+US groups to the MNs+$BaTiO_3$@Au+US group, confirming that exosome mediated repair signaling drives functional epithelial barrier re-establishment (**Fig. S22**). The iNOS/CD206 dual-label immunofluorescence revealed that MNs+US alone, despite containing exosomes, failed to induce M2 polarization due to negligible core degradation without ROS; in contrast, MNs+$BaTiO_3$+US triggered partial exosome release via $BaTiO_3$-generated ROS, leading to iNOS suppression and CD206 upregulation, confirming exosome-driven macrophage reprogramming. The MNs+$BaTiO_3$@Au+US group exhibited near complete absence of both iNOS and CD206, indicating resolution of macrophage activity and progression to full tissue repair (**Fig. 7(d, h)**). This stepwise transition demonstrates that the exosome-mediated M1 to M2 shift is a direct immunomodulatory effect, not a secondary consequence of bacterial clearance. Collectively, these findings establish ultrasound-activated cascade responsive core-shell microneedles as a promising therapeutic strategy for bacterial keratitis.

4 Conclusions

In summary, we fabricated ultrasound-activated cascade responsive core-shell microneedles that synergistically eradicate bacterial and accelerate wound healing for keratitis therapy. The piezoelectric BaTiO3@Au nanoparticles in the shell of the microneedles could generate ROS, including under ultrasound irradiation ·OH and $^1O_2$, which exhibited enhanced bacterial killing ability. Besides, the ROS responsive HAPBA/PVA hydrogel core could neutralize residual ROS and release loaded MSCs exosomes, which could suppress inflammation, and promote tissue regeneration. Crucially, in a rat keratitis model, the MNs+$BaTiO_3$@Au+US group demonstrated superior efficacy in mitigating corneal opacification, epithelial defects, and inflammatory infiltration. This work provides a promising platform for coordinated antimicrobial and immunomodulatory therapy, offering significant clinical potential for treating ocular infections and related biomedical applications.

Electronic Supplementary Material: Supplementary material (the experimental section, the ^{1}HNMR (b) and FTIR (c) of HA and HAPBA, the representative HE and tunel/DAPI staining images of rat cornea before and after MNs insertion, the representative confocal Z- stack images of a rat cornea immediately after insertion and removal of a rhodamine B-labeled core- shell microneedle, the ROS level and exosome concentration in the bacteria infected cornea at different time points after treatment with MNs and US, the EDS mapping shows the element composition of $BaTiO_3$@Au NP, the XPS spectra and UV-vis spectrum of $BaTiO_3$@Au NPs, the size and zeta potential of $BaTiO_3$ and $BaTiO_3$@Au NPs, the Live/Dead staining images of HCECs and HKs after treatment with the microneedles at varied BaTiO3@Au concentrations for 3 days, the in vivo fluorescence imaging of Cy5.5-labeled $BaTiO_3$@Au nanoparticles injected into the rat corneal stroma, the histological and immunohistochemical assessment of corneas one month after intracorneal injection of $BaTiO_3$@Au nanoparticles compared to untreated normal controls, the representative agar plate photographs and Live/Dead fluorescence images showing MRSA colonies recovered after treatment with the indicated conditions, and quantitative analysis of bacterial survival viability, the characterization of MSCs derived exosomes, the representative HE staining images of heart, liver, spleen, lung, and kidney from normal rats (control), US only, and rats subcutaneously implanted with $BaTiO_3$@Au incorporated microneedle for 2 weeks, the representative images of the central corneal endothelium acquired immediately after different treatment, including untreated control, ultrasound alone, and MNs+$BaTiO_3$@Au+US, the representative agar plate photographs showing bacterial colonies recovered from infected rat corneas after 7 days of treatment, the representative collagen and ZO-1 immunofluorescence staining images of infected cornea.) is available in the online version of this article at https://doi.org/10.26599/NR.2026.94908838.

Data availability

All data needed to support the conclusions in the paper are presented in the manuscript and/or the Electronic Supplementary Material. Additional data related to this paper may be requested from the corresponding author upon request.

Acknowledgements

This work was supported by the National Natural Science Foundation of China (82571169), the Shenzhen Medical Research Fund (B2401006 and A2303017), the Guangdong Basic and Applied Basic Research Foundation (2024A1515010457), the Jiangsu Provincial Natural Science Foundation (BK20250236), the Shenzhen Science and Technology Program (JCYJ20240813175800001), the Youth S&T Talent Support Programme of Guangdong Provincial Association for Science and Technology (SKXRC2025238), and the Scientific Foundation for Youth Scholars of Shenzhen University (868-000008010308).

Declaration of competing interest

All the contributing author(s) report(s) no conflict of interests in this work.

Author contribution statement

Bin Kong: Data curation, writing manuscript, experimental design. Taige Chen: Data curation. Qin Chen: Project administration. Rui Liu: Project administration, funding acquisition, writing manuscript. Tiantian Kong: Project administration, funding acquisition, writing manuscript. Yuanjin Zhao: Project administration, funding acquisition, writing manuscript. All the authors have approved the final manuscript.

Informed consent

Not applicable.

Ethics statement

The animal experiments were carried out following the guidelines of the Institutional Animal Care and Use Committee of Shenzhen University Medical School and were approved by the Institutional Animal Care and Use Committee of Shenzhen University Medical School (Ethical code: No. IACUC-202300142).

Use of AI statement

None.

References

[1] Ma, Y.; Chen, Y.; Wang, S.; Chen, Z. H.; Zhang, Y.; Huang, L.; Zhang, X.; Yin, F.; Wang, Y.; Yang, M.; Li, Z.; Huang, K.; Fang, X.; Li, Z.; Wang, M.; Liu, W.; Li, J. N.; Li, L.; Zhao, H.; Wei, M.; Shi, Y.; Liu, R.; Zhang, M.; Chen, J.; Shen, J.; Meng, J.; Yang, Y.; Zhang, F.; Gong, X.; Han, G.; Xue, T., Near-infrared spatiotemporal color vision in humans enabled by upconversion contact lenses. *Cell* **2025**, *188* (13), 3375-3388 e3318.

[2] Yang, Y.; Wang, Y.; Zhu, C.; Xie, Z.; Qin, Z.; Wang, Z.; Chai, Y., Bioinspired and biointegrated vision for artificial sight convergence. *Nat. Rev. Bioeng.* **2025**, *3*, 939–954.

[3] Wang, L.; Guo, Y.; Chen, B.; Lu, S.; Yang, J.; Jin, Y.; Wang, X.; Sun, X.; Wang, S.; Wang, B., An annular corneal microneedle patch for minimally invasive ophthalmic drug delivery. *Sci. Adv.* **2025**, *11* (10), eadv1661.

[4] Zhang, H.; Li, D.; Ren, H.; Ma, Z.; Meng, S.; Qiao, Y.; Yang, J.; Wang, Y.; Zhou, Q.; Xie, L., A Bioinspired Virus-Like Mechano-Bactericidal Nanomotor for Ocular Multidrug-Resistant Bacterial Infection Treatment. *Adv. Mater.* **2025**, *37* (8), e2408221.

[5] Qian, S.; Wang, X.; Guo, Y.; He, W.; Yang, J.; Chen, H.; Li, R.; Su, L.; Wang, X.; Shao, Y.; Wang, B., Synchronous Sterilization and Immunoreaction Termination for Corneal Transparency Protection in Treating Pseudomonas aeruginosa Induced Bacterial Keratitis. *Adv. Mater.* **2025**, *37* (20), e2419209.

[6] Li, B.; Ma, R.; Chen, L.; Zhou, C.; Zhang, Y. X.; Wang, X.; Huang, H.; Hu, Q.; Zheng, X.; Yang, J.; Shao, M.; Hao, P.; Wu, Y.; Che, Y.; Li, C.; Qin, T.; Gao, L.; Niu, Z.; Li, Y., Diatomic iron nanozyme with lipoxidase-like activity for efficient inactivation of enveloped virus. *Nat. Commun.* **2023**,

14 (1), 7312.

[7] Choi, V.; Rohn, J. L.; Stoodley, P.; Carugo, D.; Stride, E., Drug delivery strategies for antibiofilm therapy. *Nat. Rev. Microbiol.* **2023**, *21* (9), 555-572.

[8] Lu, Z.; Fan, W.; Ye, Y.; Huang, Y.; Zhou, X.; Zhang, Y.; Cui, W.; Ji, J.; Yao, K.; Han, H., Drug in Drug: Quorum Sensing Inhibitor in Star-Shaped Antibacterial Polypeptides for Inhibiting and Eradicating Corneal Bacterial Biofilms. *ACS Nano* **2025**, *19* (2), 2268-2285.

[9] Huang, J.; Jiang, T.; Qie, J.; Cheng, X.; Wang, Y.; Ye, Y.; Yang, Z.; Yan, H.; Yao, K.; Han, H., Biologically inspired bioactive hydrogels for scarless corneal repair. *Sci. Adv.* **2024**, *10* (51), eadt1643.

[10] Costley, D.; Mc Ewan, C.; Fowley, C.; McHale, A. P.; Atchison, J.; Nomikou, N.; Callan, J. F., Treating cancer with sonodynamic therapy: a review. *Int. J. Hyperthermia* **2015**, *31* (2), 107-117.

[11] Yang, F.; Dong, J.; Li, Z.; Wang, Z., Metal-Organic Frameworks (MOF)-Assisted Sonodynamic Therapy in Anticancer Applications. *ACS Nano* **2023**, *17* (5), 4102-4133.

[12] Geng, C.; He, S.; Yu, S.; Johnson, H. M.; Shi, H.; Chen, Y.; Chan, Y. K.; He, W.; Qin, M.; Li, X.; Deng, Y., Achieving Clearance of Drug-Resistant Bacterial Infection and Rapid Cutaneous Wound Regeneration Using an ROS-Balancing-Engineered Heterojunction. *Adv. Mater.* **2024**, *36* (16), e2310599.

[13] Wen, B.; Huang, D.; Song, C.; Chen, Y.; Zhao, Y., Ultrasound-Responsive Microcapsules Delivering Oxygen and Traditional Chinese Medicine for Wound Healing. *Smart Med.* **2025**, *4* (4), e70021.

[14] Qian, X.; Zheng, Y.; Chen, Y., Micro/Nanoparticle-Augmented Sonodynamic Therapy (SDT): Breaking the Depth Shallow of Photoactivation. *Adv. Mater.* **2016**, *28* (37), 8097-8129.

[15] Shuai, C.; Liu, G.; Yang, Y.; Qi, F.; Peng, S.; Yang, W.; He, C.; Wang, G.; Qian, G., A strawberry-like Ag-decorated barium titanate enhances piezoelectric and antibacterial activities of polymer scaffold. *Nano Energy* **2020**, *74*, 104825.

[16] Kong, B.; Liu, R.; Hu, X.; Li, M.; Zhou, X.; Zhao, Y.; Kong, T., Cornea-Inspired Ultrasound - Responsive Adhesive Hydrogel Patches for Keratitis Treatment. *Adv. Funct. Mater.* **2023**, *34* (12), 2310544.

[17] Shang, S.; Zheng, F.; Tan, W.; Xing, Z.; Chen, S.; Peng, F.; Lv, X.; Wang, D.; Zhu, X.; Wu, J.; Zhou, Z.; Zhang, X.; Yang, X., Piezoelectric Biomaterial with Advanced Design for Tissue Infection Repair. *Adv. Sci.* **2025**, *12* (10), e2413105.

[18] Harrell, C. R.; Jovicic, N.; Djonov, V.; Arsenijevic, N.; Volarevic, V., Mesenchymal Stem Cell-Derived Exosomes and Other Extracellular Vesicles as New Remedies in the Therapy of Inflammatory Diseases. *Cells* **2019**, *8* (12), 1605.

[19] Willis, G. R.; Fernandez-Gonzalez, A.; Anastas, J.; Vitali, S. H.; Liu, X.; Ericsson, M.; Kwong, A.; Mitsialis, S. A.; Kourembanas, S., Mesenchymal Stromal Cell Exosomes Ameliorate Experimental Bronchopulmonary Dysplasia and Restore Lung Function through Macrophage Immunomodulation. *Am. J. Respir Crit. Care Med.* **2018**, *197* (1), 104-116.

[20] Liao, Z.; Luo, R.; Li, G.; Song, Y.; Zhan, S.; Zhao, K.; Hua, W.; Zhang, Y.; Wu, X.; Yang, C., Exosomes from mesenchymal stem cells modulate endoplasmic reticulum stress to protect against nucleus pulposus cell death and ameliorate intervertebral disc degeneration in vivo. *Theranostics* **2019**, *9* (14), 4084-4100.

[21] Phinney, D. G.; Pittenger, M. F., Concise Review: MSC-Derived Exosomes for Cell-Free Therapy. *Stem Cells* **2017**, *35* (4), 851-858.

[22] Liu, J.; Gao, J.; Lu, P.; Wang, Y.; Xing, S.; Yan, Y.; Han, R.; Hao, P.; Li, X., Mesenchymal Stem Cell-Derived Exosomes as Drug Carriers for Delivering miRNA-29b to Ameliorate Inflammation in Corneal Injury Via Activating Autophagy. *Invest. Ophthalmol. Vis. Sci.* **2024**, *65* (6), 16.

[23] Sanghani, A.; Andriesei, P.; Kafetzis, K. N.; Tagalakis, A. D.; Yu-Wai-Man, C., Advances in exosome therapies in ophthalmology-From bench to clinical trial. *Acta Ophthalmol.* **2022**, *100* (3), 243-252.

[24] Liu, J.; Jiang, F.; Jiang, Y.; Wang, Y.; Li, Z.; Shi, X.; Zhu, Y.; Wang, H.; Zhang, Z., Roles of Exosomes in Ocular Diseases. *Int. J. Nanomedicine* **2020**, *15*, 10519-10538.

[25] Zhang, Z.; Shi, H.; Chen, J.; Gu, R.; Li, Y.; Huai, S.; Li, S.; Hu, Y.; Wei, H.; Lin, D.; Lei, L.; Bao, Z.; Wang, J.; Li, X., Highly Efficient Intrastromal Dual-Drug Delivery by a Dissolving Bilayer Microneedle for Synergistic Therapy against Corneal Neovascularization. *ACS Nano* **2025**, *19* (42), 37065-37081.

[26] Jiang, X.; Jin, Y.; Zeng, Y.; Shi, P.; Li, W., Self-Implantable Core-Shell Microneedle Patch for Long-Acting Treatment of Keratitis via Programmed Drug Release. *Small* **2024**, *20* (29), e2310461.

[27] Yu, F.; Zhao, X.; Wang, Q.; Fang, P. H.; Liu, L.; Du, X.; Li, W.; He, D.; Zhang, T.; Bai, Y.; Liu, L.; Li, S.; Yuan, J., Engineered Mesenchymal Stromal Cell Exosomes-Loaded Microneedles Improve Corneal Healing after Chemical Injury. *ACS Nano* **2024**, *18* (31), 20065-20082.

[28] Zhang, J.; Shi, Y.; Zhang, Y.; Fang, Z.; Zhou, Y.; Bian, F.; Zhang, Y.; Sun, W., Antibacterial and Proangiogenic Hydrogel Microneedle Patches for Wound Healing. *Smart Med.* **2025**, *4* (3), e70014.

[29] Song, C.; Lu, M.; Li, N.; Gu, H.; Li, M.; Lu, L.; Wang, Y., MXene-Integrated Responsive Hydrogel Microneedles for Oral Ulcers Healing. *Smart Med.* **2025**, *4* (1), e135.

[30] Fan, L.; Wang, L.; Wang, X.; Li, M.; Gu, H.; Zhang, H., Multifunctional Silk and Gelatin Composed Microneedle Patches for Enhanced Wound Healing. *Smart Med.* **2025**, *4* (1), e137.

[31] Sullivan, S. P.; Koutsonanos, D. G.; Del Pilar Martin, M.; Lee, J. W.; Zarnitsyn, V.; Choi, S. O.; Murthy, N.; Compans, R. W.; Skountzou, I.; Prausnitz, M. R., Dissolving polymer microneedle patches for influenza vaccination. *Nat. Med.* **2010**, *16* (8), 915-920.

[32] Kusama, S.; Sato, K.; Matsui, Y.; Kimura, N.; Abe, H.; Yoshida, S.; Nishizawa, M., Transdermal electroosmotic flow generated by a porous microneedle array patch. *Nat. Commun.* **2021**, *12* (1), 658.

[33] Tehrani, F.; Teymourian, H.; Wuerstle, B.; Kavner, J.; Patel, R.; Furmidge, A.; Aghavali, R.; Hosseini-Toudeshki, H.; Brown, C.; Zhang, F.; Mahato, K.; Li, Z.; Barfidokht, A.; Yin, L.; Warren, P.; Huang, N.; Patel, Z.; Mercier, P. P.; Wang, J., An integrated wearable microneedle array for the continuous monitoring of multiple biomarkers in interstitial fluid. *Nat. Biomed. Eng.* **2022**, *6* (11), 1214-1224.

[34] Jiang, X.; Liu, S.; Chen, J.; Lei, J.; Meng, W.; Wang, X.; Chu, Z.; Li, W., A Transformative Wearable Corneal Microneedle Patch for Efficient Therapy of Ocular Injury and Infection. *Adv. Sci.* **2025**, *12* (12), e2414548.

[35] Huynh, A.; Priefer, R., Hyaluronic acid applications in ophthalmology, rheumatology, and dermatology. *Carbohydr. Res.* **2020**, *489*, 107950.

[36] Onugwu, A. L.; Nwagwu, C. S.; Onugwu, O. S.; Echezona, A. C.; Agbo, C. P.; Ihim, S. A.; Emeh, P.; Nnamani, P. O.; Attama, A. A.; Khutoryanskiy, V. V., Nanotechnology based drug delivery systems for the treatment of anterior segment eye diseases. *J. Control. Release* **2023**, *354*, 465-488.

[37] Yuan, R.; Du, S.; Pan, S.; Lin, Z.; Zhang, N.; Zhang, C.; Zeng, Q.; Wei, Y.; Wu, Y.; Tao, L., Multifunctional hydrogel encapsulated with baicalin for full-layer regeneration of drug-resistant bacteria-infected wounds after radiotherapy. *Bioact. Mater.* **2025**, *53*, 20-31.

[38] Qin, W.; Ma, Z.; Bai, G.; Qin, W.; Li, L.; Hao, D.; Wang, Y.; Yan, J.; Han, X.; Niu, W.; Niu, L.; Jiao, K., Neurovascularization inhibiting dual responsive hydrogel for alleviating the progression of osteoarthritis. *Nat. Commun.* **2025**, *16* (1), 1390.

[39] Zhang, A.; Zeng, Y.; Xiong, B.; Jiang, X.; Jin, Y.; Wang, S.; Yuan, Y.; Li, W.; Peng, M., A pH-Responsive Core-Shell Microneedle Patch with Self - Monitoring Capability for Local Long - Lasting Analgesia. *Adv. Funct. Mater.* **2023**, *34* (12), 2314048.

[41] Li, H.; Zheng, X.; Gao, Z.; Mu, T.; Liu, M.; Li, J.; Wu, J.; Zhang, W.; Lee, C. S.; Liu, W.; Wang, P., ROS - Responsive Core - Shell Microneedles Based on Simultaneous Efficient Type I/II Photosensitizers for Photodynamic Against Bacterial Biofilm Infections. *Adv. Funct. Mater.* **2024**, *35* (21), 2401477.

[41] Zhang, Y.; Wang, S.; Yang, Y.; Zhao, S.; You, J.; Wang, J.; Cai, J.; Wang, H.; Wang, J.; Zhang, W.; Yu, J.; Han, C.; Zhang, Y.; Gu, Z., Scarless wound healing programmed by core-shell microneedles. *Nat. Commun.* **2023**, *14* (1), 3431.

[42] Kim, H.; Lee, J.; Heo, U.; Jayashankar, D. K.; Agno, K. C.; Kim, Y.; Kim, C. Y.; Oh, Y.; Byun, S. H.; Choi, B.; Jeong, H.; Yeo, W. H.; Li, Z.; Park, S.; Xiao, J.; Kim, J.; Jeong, J. W., Skin preparation-free, stretchable

microneedle adhesive patches for reliable electrophysiological sensing and exoskeleton robot control. *Sci. Adv.* **2024**, *10* (3), eadk5260.

[43] Yang, Z. R.; Suo, H.; Fan, J. W.; Lv, N.; Du, K.; Ma, T.; Qin, H.; Li, Y.; Yang, L.; Zhou, N.; Jiang, H.; Tao, J.; Zhu, J., Endogenous stimuli-responsive separating microneedles to inhibit hypertrophic scar through remodeling the pathological microenvironment. *Nat. Commun.* **2024**, *15* (1), 2038.

[44] Zheng, B.; Li, Q.; Fang, L.; Cai, X.; Liu, Y.; Duo, Y.; Li, B.; Wu, Z.; Shen, B.; Bai, Y.; Cheng, S. X.; Zhang, X., Microorganism microneedle micro-engine depth drug delivery. *Nat. Commun.* **2024**, *15* (1), 8947.

[45] Kong, B.; Liu, R.; Shan, J.; Li, M.; Zhou, X.; Zhao, Y., Frozen reinforced microneedles loaded with NIR-photothermal nanozyme for keratitis treatment. *Nano Today* **2023**, *52*, 102000.

[46] Zhao, J.; Jia, F.; Li, J.; Tao, Y. C.; Hu, J. Y.; Ren, K. F.; Ji, J.; Fu, J. Y.; Fu, G. S.; Huang, H., Sprayable Reactive Oxygen Species-Responsive Hydrogel Coatings Restore Endothelial Barrier Integrity for Functional Vascular Healing. *ACS Nano* **2025**, *19* (23), 21757-21774.

[47] Cao, J.; Zhang, X.; Guo, J.; Wu, J.; Lin, L.; Lin, X.; Mu, J.; Huang, T.; Zhu, M.; Ma, L.; Zhou, W.; Jiang, X.; Wang, X.; Feng, S.; Gu, Z.; Gao, J. Q., An engineering-reinforced extracellular vesicle-integrated hydrogel with an ROS-responsive release pattern mitigates spinal cord injury. *Sci. Adv*. **2025**, *11* (14), eads3398.

[48] Liu, Y.; Yang, X.; Wu, K.; Feng, J.; Zhang, X.; Li, A.; Cheng, C.; Zhu, Y. Z.; Guo, H.; Wang, X., Skin-Inspired and Self-Regulated Hydrophobic Hydrogel for Diabetic Wound Therapy. *Adv. Mater*. **2025**, *37* (16), e2414989.

[49] Zhang, X.; Lyu, Y.; Liu, Y.; Yang, R.; Liu, B.; Li, J.; Xu, Z.; Zhang, Q.; Yang, J.; Liu, W., Artificial apoptotic cells/VEGF-loaded injectable hydrogel united with immunomodification and revascularization functions to reduce cardiac remodeling after myocardial infarction. *Nano Today* **2021**, *39*, 101227.

[50] Wen, Z.; Li, S.; Liu, Y.; Liu, X.; Qiu, H.; Che, Y.; Bian, L.; Zhou, M., An engineered M2 macrophage-derived exosomes-loaded electrospun biomimetic periosteum promotes cell recruitment, immunoregulation, and angiogenesis in bone regeneration. *Bioact. Mater.* **2025**, *50*, 95-115.

[51] Liu, J.; Li, Z., Resident Innate Immune Cells in the Cornea. *Front Immunol.* **2021**, *12*, 620284.

[52] Downie, L. E.; Zhang, X.; Wu, M.; Karunaratne, S.; Loi, J. K.; Senthil, K.; Arshad, S.; Bertram, K.; Cunningham, A. L.; Carnt, N.; Mueller, S. N.; Chinnery, H. R., Redefining the human corneal immune compartment using dynamic intravital imaging. *Proc. Natl. Acad. Sci. U. S. A.* **2023**, *120* (31), e2217795120.

[53] Colorado, L. H.; Edwards, K.; Chinnery, H. R.; Bazan, H. E., In vivo immune cell dynamics in the human cornea. *Exp. Eye Res*. **2020**, *199*, 108168.

[54] Wang, X.; Han, C.; Xia, J.; Cui, C.; Min, P.; Meng, X.; Sun, Y.; Wen, K.; Feng, C.; Zhang, Y.; Li, K., Ultrasound-Mediated Piezoelectric Microneedles Regulating Macrophage Polarization and Remodeling Pathological Microenvironment for Lymphedema Improvement. *ACS Nano* **2025**, *19* (1), 1447-1462.

[55] Wang, Y.; Zhou, C.; Li, Z.; Li, G.; Zou, Y.; Li, X.; Gu, P.; Liu, J.; Bai, L.; Yan, H.; Liang, J.; Zhang, X.; Fan, Y.; Sun, Y., Injectable immunoregulatory hydrogels sequentially drive phenotypic polarization of macrophages for infected wound healing. *Bioact. Mater*. **2024**, *41*, 193-206.

Electronic Supplementary Material

Ultrasound responsive microneedles for sequential antibacterial and immune regulation in keratitis treatment

Bin Kong[1], Taige Chen[1], Qin Chen[2], Rui Liu[1,2], Tiantian Kong[1], and Yuanjin Zhao[2]

[1] *School of Biomedical Engineering, Shenzhen University Medical School, Shenzhen University, Shenzhen 518060, China*
[2] *Department of Rheumatology and Immunology, Nanjing Drum Tower Hospital, School of Biological Science and Medical Engineering, Southeast University, Nanjing 210096, China*

Address correspondence to Yuanjin Zhao, yjzhao@seu.edu.cn; Tiantian Kong, ttkong@szu.edu.cn; Rui Liu, liur16_thu@foxmail.com; Qin Chen, chenqin0331@163.com

Supporting information to https://doi.org/10.26599/NR.2026.94908838

Experimental Section

Materials

PVA was bought from Jiangsu JL and Biotech Corporation (China). FITC-BSA, rhodamine B, DiD, and DCFH-DA were provided by Solarbio (China). Other chemical materials not mentioned were bought from Sigma-Aldrich (USA). S. aureus and P. aeruginosa were purchased from ATCC (USA). The cell culture and staining-related materials, including Dulbeccoo's modified Eagle's medium (DMEM), Fetal Bovine Serum (FBS), Penicillin-Streptomycin (PS), trypsin, phalloidin, and 4', 6-diamidino-2-phenylindole (DAPI) were bought from Gibco (USA). Syto/PI staining kit, cell Live/dead essay and CCK-8 kit were bought from Jiangsu KeyGEN BioTECH Corp (China). Primary antibodies of CD 9, CD 63, TSG 101, and iNOS were obtained from Abcam (USA). The primary antibodies of IL-6, TNF-α, α-SMA, CD 68, CD 206, and F4/80 were bought from Proteintech (USA). The secondary antibodies of Alexa Fluor 488 goat anti-rabbit IgG H&L, Alexa Fluor 594 goat anti-rabbit IgG H&L, and HRP-conjugated goat anti-rabbit IgG H&L were bought from Abcam (USA).

Synthesis of HAPBA

The HAPBA was prepared according to previously reported method [1, 2]. 500 mg HA was dissolved in 100 mL ddH$_2$O, followed by the addition of 150 mg 3-aminophenylboronic acid (APBA) and vigorous stir. Then, 200 mg 4-(4,6-Dimethoxy-1,3,5-triazin-2-yl)-4-methylmorpholinium chloride (DMTMM) was added and continuously stirred for 24 hours. Finally, the mixtures were dialyzed (MWCO 3500), freeze dried, and stored at 2-8 ° C before use. ^{1}HNMR and FTIR were used to confirm the chemical structure of HAPBA.

Fabrication and characterization of the core-shell microneedles

10 wt% HA solution was cast into a polydimethylsiloxane (PDMS) mold. Vacuum application facilitated complete infiltration of the solution into the microcavities, ensuring formation of the MN tips. Subsequent overnight air-drying at ambient temperature yielded the HA shell structure. The hollow MN array was then infused with a mixed solution containing PVA and HAPBA (volume ratio 1:1) through the assistance of vacuum. Following overnight drying at room temperature, the core-shell structured microneedles could be obtained. The morphology of the resulting core-shell microneedles were analyzed using an SEM (ZEISS) and confocal laser scanning microscopy (CLSM, Olympus).

For the preparation of the ultrasound-responsive shell, BaTiO$_3$@Au nanoparticles (200 μg/mL) were first dispersed in a 10 wt% HA aqueous solution by ultrasonication for 10 min to ensure homogeneous distribution. For the core component, MSC-derived exosomes were thawed on ice and gently mixed into a pre-gelled solution of PVA and HAPBA to a final exosome concentration of 50 μg/ mL.

The mechanical integrity of core-shell microneedles fabricated with HAPBA concentrations of 1%, 2%, and 3% was evaluated using an Instron universal testing machine. The microneedles were positioned with their tips oriented vertically downward on the stationary lower clamp. Axial force was applied to the baseplate of the microneedle array via the movable upper clamp at a constant displacement rate of 1 mm/min until structural failure occurred.

The H$_2$O$_2$-triggered release kinetics from the microneedles were characterized using FITC-BSA (initial loading: 1 mg/mL) encapsulated within the core. The microneedle patches were incubated in phosphate-buffered saline (PBS) solutions containing varying H$_2$O$_2$ concentrations (0, 0.1, 0.5, and 1 mM) under constant agitation (300 rpm) at 37 ° C using an Eppendorf thermomixer. At predetermined intervals, 100 μL samples were collected from the release medium and immediately replenished with an equal volume of fresh PBS containing corresponding H$_2$O$_2$ concentrations to preserve sink conditions. FITC-BSA fluorescence in aliquots was determined using a Thermo Scientific Multiskan GO microplate reader (excitation wavelength 493 nm and emission wavelength 550 nm). Cumulative FITC-BSA release profiles were derived by correlating the measured fluorescence intensities with a pre-established standard curve.

Rhodamine B (rhB, 0.1 mg/mL) was dissolved with HA to prepare a fluorescently labeled shell solution. Core-shell MNs with rhB labeled shell were fabricated using the same protocol as the therapeutic MNs. Freshly enucleated rat eyes were rinsed with sterile PBS, and the corneas were kept moist. Under a stereomicroscope, a single rhB labeled MN array was gently pressed into the central cornea with the same force as in the animal experiments (held for 30 s). The MNs were then carefully lifted off, and the corneas were immediately placed epithelial side down onto a confocal dish. Confocal Z-stack images were acquired using an Olympus FV3000 confocal microscope from the surface (0 μm) to 200 μm depth.

Preparation and characterization of $BaTiO_3$@Au NPs

$BaTiO_3$@Au NPs were synthesized following a modified literature protocol [3, 4]. Briefly, 500 mg of $BaTiO_3$ powder was dispersed in 100 mL of dH_2O. Subsequently, 2 mL of ammonium hydroxide ($NH_3 \cdot H_2O$) was added, followed by dropwise addition of 5 mL of an aqueous hydrogen tetrachloroaurate trihydrate ($HAuCl_4 \cdot 3H_2O$) solution (Au^{3+} concentration: 10 mg/mL). The resulting suspension was vigorously stirred. The product was collected via centrifugation and finally calcined at 300 ° C for 1 hour to yield the $BaTiO_3$@Au NPs.

The microscopic morphology of $BaTiO_3$ and $BaTiO_3$@Au was determined by SEM and TEM. EDS mapping was performed to detect the element of BaTiO3@Au. The hydrodynamic diameter and zeta potential of the $BaTiO_3$ and $BaTiO_3$@Au were determined by dynamic light scattering (DLS, Malvern Zetasizer Nano ZS90). XPS spectra were obtained by a XPS spectrometer (K-Alpha, Thermo Scientific).

ROS generation of $BaTiO_3$@Au NPs

Electron spin resonance (ESR) spectroscopy was employed to confirm ROS generation using a Bruker E500 spectrometer (Billerica, MA). 5,5-Dimethyl-1-pyrroline N-oxide (DMPO) and 2,2,6,6-tetramethyl-4-piperidine (TEMP) served as spin-trapping agents for hydroxyl radicals (·OH) and singlet oxygen ($^1O_2$), respectively. Samples (0.5 mM of $BaTiO_3$ or $BaTiO_3$@Au NPs) were analyzed under ultrasonic irradiation (1.5 W/cm^2, 1 MHz).

Ex vivo evaluation of temporal cascade of ROS and exosome release in infected corneas

To establish an authentic infected microenvironment and verify the sequential cascade, freshly harvested rat eyes were used. The corneas were excised under a surgical microscope, and the central epithelium was gently scraped off with a sterile scalpel. A 20 μL droplet of S. aureus suspension (1x10^7 CFU/mL in PBS) was applied to the corneal surface and incubated at 37 ° C for 24 h to establish a localized infection. After rinsing with sterile PBS, the infected corneas were mounted epithelial side up on a bed of 1% agarose in a 6-well plate.

The core-shell microneedle with $BaTiO_3$@Au nanoparticles and MSC-derived exosomes were inserted into the central cornea by gentle manual pressure. A thin layer of ultrasound coupling gel was applied, and US was delivered perpendicularly using a transducer (1.5 W/cm^2, 1 MHz) for 5 min. Immediately after US treatment, the MNs were carefully lifted off, and the corneas were transferred to pre-warmed DMEM and cultured at 37 ° C in a humidified incubator. At precisely defined intervals post-US (0, 1, 2, 3, 6, and 12 h), corneal tissues were harvested, briefly rinsed in PBS, blotted dry, weighed, snap-frozen in liquid nitrogen, and stored at -80 ° C until analysis.

Each frozen cornea was minced and homogenized in 200 μL of PBS containing protease inhibitors (Roche) using a tissue grinder. The homogenate was centrifuged at 12,000 g for 10 min at 4 ° C, and the supernatant was collected. For the detection of intracellular/extracellular ROS, 100 μL of the supernatant was mixed with 10 μM DCFH-DA and incubated at 37 ° C in the dark for 30 min. The fluorescence intensity was measured using a microplate reader (excitation 488 nm, emission 525 nm). ROS levels were expressed as arbitrary fluorescence units (a.u.), and all measurements were performed in triplicate.

The concentration of MSC-derived exosomes released into the cornea was quantified using a commercial BCA protein quantification kit following the manufacturer's instructions. In brief, exosomes were first isolated from corneal tissue homogenates at each time point by ultracentrifugation to remove tissue debris and other impurities. After centrifugation, 100 μL of the exosome-containing supernatant or serially diluted BSA standards were added to the wells of a 96-well plate. Then, 100 μL of the BCA working solution was added to each well, and the plate was incubated for 30 min at 37 ° C in the dark. The absorbance was read at 562 nm using a microplate reader. The total protein concentration in each exosome-containing supernatant was derived from a standard curve and normalized to the initial corneal tissue wet weight, giving the final exosome concentration as μg of exosome protein per mL of supernatant.

In vitro biocompatibility evaluation

HCECs and HKs were cultured for 72 hours in transwell systems containing $BaTiO_3$@Au NPs-incorporated microneedles (0, 50, 100, 200 μg/mL). Cellular viability was assessed via calcein AM/ethidium homodimer staining (Live/Dead assay) using fluorescence microscopy (Leica, Germany).

To assess long-term ocular safety, a separate cohort of SD rats received intracorneal injection of $BaTiO_3$@Au nanoparticles (200 μg/mL, 5 μL) as described above. One month later, the rats were euthanized and the corneas were harvested, fixed in 4% paraformaldehyde, and embedded in paraffin. Sections were subjected to HE and Masson's trichrome staining for morphological and collagen assessment. For immunohistochemistry, deparaffinized sections were incubated with primary antibodies against interleukin-6 (IL-6, Proteintech) and tumor necrosis factor-α (Proteintech), followed by HRP-conjugated secondary antibodies and DAB chromogen detection. Normal untreated corneas were processed in parallel as controls.

In vivo tracking of nanoparticle clearance in the cornea

Male Sprague-Dawley rats (6 weeks old) were anesthetized with isoflurane and received topical 0.5% lidocaine hydrochloride. Under a surgical microscope, 5 μL of Cy5.5-labeled $BaTiO_3$@Au nanoparticle suspension (200 μg/mL in sterile PBS) was injected into the central corneal stroma. The contralateral eye served as an untreated control. At predetermined time points post-injection (0, 1, 3, and 7 d), the rats were anesthetized and imaged using an in vivo imaging system (IVIS Spectrum, PerkinElmer) with excitation/emission filters of 675/720 nm. Fluorescence intensity in a circular region of interest covering the cornea was quantified (Living Image software). All data were expressed as the percentage of initial signal at day 0 after background subtraction.

Ultrasound Irradiation Protocol

US irradiation was performed using a Sonoplus 190 ultrasound generator (Enarf-Nonius, Holland) equipped with a flat-surface probe (diameter: 1.0 cm, effective radiating area: 0.785 cm^2) . The transducer was operated at a frequency of 1 MHz, intensity of 1.5 W/cm^2, in pulsed wave mode with a duty cycle of 50% (pulse duration: 5 ms, pulse repetition period: 10 ms) , for 5 minutes per treatment session. For both in vitro and in vivo experiments, US coupling gel (Aquasonic 100, Parker Laboratories) was applied between the probe surface and the sample to ensure efficient acoustic transmission. The probe was placed in direct contact with the coupling gel layer, maintaining a probe to target distance of approximately 3-5 mm.

For in vivo corneal ultrasound treatment, rats were anesthetized with isoflurane and corneas received topical 0.5% lidocaine hydrochloride. The eyelid of the infected eye was gently closed to create a smooth, convex surface over the cornea. Ultrasound coupling gel was generously applied to the external surface of the closed eyelid to ensure acoustic impedance matching and eliminate air gaps. The flat-surface ultrasound probe was positioned perpendicular to the corneal plane and placed in direct, gentle contact with the coupling gel layer, not in direct contact with the eyelid tissue, maintaining a probe to corneal surface distance of approximately 3-5 mm. This standoff geometry ensures that the distal margin of the ultrasound near-field zone encompasses the entire corneal area while avoiding mechanical compression of the globe. Ultrasonic irradiation was delivered using the parameters described above. After treatment, the coupling gel was gently wiped off with a sterile cotton swab. All procedures were performed by the same operator to ensure consistency.

In vitro antibacterial experiments

For the preparation of $BaTiO_3$ or $BaTiO_3$@Au incorporated microneedles, 100 μg/mL $BaTiO_3$ or $BaTiO_3$@Au was dispersed in the HA solution. *S. aureus* and *P. aeruginosa* were used for the evaluation of the antibacterial effect. 1 mL bacteria with a density of 2x10^6 CFU/mL were incubated with 100 μL MNs; MNs+$BaTiO_3$, and MNs+$BaTiO_3$@Au for 1 hour and with US stimulation (1.5 W/cm^2, 1 MHz) for 5 min, respectively. The bacteria without treatment was used as a control. After incubating, 100 μL of diluted bacterial suspension were streaked onto agar plates and incubated.

A clinically isolated strain of methicillin-resistant *S. aureus* (MRSA, ATCC 43300) was cultured, harvested, and resuspended in sterile PBS to a final concentration of 2x10^6 CFU/mL. To compare the antibacterial efficacy with a standard of care antibiotic, three treatment groups were established: (i) untreated control (bacteria in PBS only), (ii) commercial antibiotic-corticosteroid eye drop group (tobramycin dexamethasone, abbreviated as Drop, incubated with bacteria for 1 h), and (iii) MNs+BaTiO3@Au+US (incubated with bacteria for 1 h followed by 5 min US irradiation at 1.5 W/cm^2, 1 MHz). After treatment, bacterial suspensions were serially diluted and spread onto agar plates for incubation.

For SEM analysis, colonies underwent ethanol gradient dehydration (30%, 50%, 70%, 90%, 95%, 100%) prior to critical point drying on silicon substrates. For viability assessment, bacteria were dual-stained with SYTO 9 and propidium iodide, washed thrice with PBS via centrifugation, and imaged by fluorescence microscopy (live: green; dead: red). Bacterial viability was quantified as: Survival viability (%) = Nl/Nt x 100 %, where Nl refers to live bacteria number and Nt represents total bacteria number.

Preparation and characterization of MSCs exosomes

MSC derived exosomes were isolated from the supernatant of the culture medium of MSCs based on an ultracentrifuge method. In brief, the MSCs culture medium was centrifuged at 10000 x g for 10 min to remove dead cells and debris cells. Then, the medium was subjected to ultracentrifugation at 110000 x g for 70 min to obtain the exosomes.

To evaluate the validation of exosome stability after microneedle encapsulation and ultrasound/ROS exposure, MSC-derived exosomes were isolated as described above and divided into three groups: (i) Exos, freshly thawed exosomes suspended in sterile PBS (100 μg/mL); (ii) MNs-Exos, exosomes extracted from freshly fabricated core-shell MNs (without US treatment). To extract exosomes, the MNs were dissolved in sterile PBS containing D-glucose (50 mM) at 37 ° C for 2 h under gentle shaking. Glucose competes with PVA for the boronic acid binding sites on HAPBA, displacing the PVA chains and leading to hydrogel network dissociation. The resulting solution was centrifuged at 2000 g for 10 min at 4 ° C to remove any residual polymer or NP debris, and the supernatant containing the released exosomes was collected; (iii) MNs+US-Exos, exosomes extracted from MNs after the full US-triggered cascade. Specifically, MNs were immersed in PBS, subjected to US irradiation (1.5 W/cm^2, 1 MHz, 5 min) to activate BaTiO3@Au and generate ROS, incubated for an additional 2 h to allow ROS-responsive core degradation and exosome release, and then processed identically to (ii).

TEM was used to visualize exosome morphology following negative staining with 3% phosphotungstic acid. Nanoparticle tracking analysis (NTA) quantified exosome size distribution and concentration. Western blot analysis was performed to confirm identity and isolation purity of exosomes using antibodies against characteristic markers (CD 63, CD 9, TSG 101) on both exosomes and MSCs. For cell uptake detection, exosomes were labeled with fluorescent lipophilic dye 1,1'-Dioctadecyl-3,3,3',3'-Tetramethylindodicarbocyanine,4-Chlorobenzenesulfonate Salt (DiD). Briefly, thawed exosomes were incubated with DiD (10 μM). Labeled exosomes were then isolated via ultracentrifugation (110000 x g, 20 min) to yield DiD-Exo.

In vitro ROS-scavenging assay

To assess exosomal antioxidant capacity, intracellular ROS levels were monitored using DCFH-DA fluorogenic probe. HCECs seeded in the confocal dish were cultured overnight. After medium removal, cells underwent 6 h co-treatment with H_2O_2 (oxidative challenge) and exosomes (25, 50, 100 μg/mL). Cells were then loaded with DCFH-DA and imaged by fluorescence microscopy. For quantitative analysis, identically treated cells in 6-well plates were trypsinized post-staining, washed thrice with PBS, and subjected to flow cytometric quantification of DCFH-DA fluorescence intensity.

Cell migration assay

For the preparation of exosomes incorporated microneedles, 50 μg/mL exosomes were dispersed in the HAPBA/PVA solution. HCECs were seeded in 12-well plates (5x10^5 cells/well) and cultured to confluence. A standardized scratch was created in the monolayer using a sterile pipette tip. After PBS washing, cells were treated with MNs and MNs+Exo. The cells were stained with AM, and wound closure was monitored after 0, 12, and 24 h via fluorescent microscopy. The residual ratio was calculated.

Analysis of macrophage polarization

The influence of exosomes on the macrophage phenotype was assessed by immunofluorescent staining and qPCR. RAW264.7

macrophages were cultured in confocal dishes (5×10^4 cells/dish) for 24 h. Cells were then primed with lipopolysaccharide (LPS, 100 ng/mL) for 12 h, followed by 24 h exposure to Exo-MNs extract. For the immunofluorescent staining, cells were fixed and incubated with primary antibodies (CD 68, iNOS, and CD 206), and then incubated with secondary antibodies. After secondary antibody removal and three PBS washes, nuclei were stained with 4',6-diamidino-2-phenylindole (DAPI).

For the qPCR, total RNA was isolated from cells using Trizol Reagent per manufacturer's protocol. RNA integrity was verified spectrophotometrically (NanoDrop™, Thermo Fisher Scientific). cDNA synthesis utilized 1 μg RNA with PrimeScript™ RT Reagent Kit. Quantitative PCR employed SYBR® Green Premix Ex Taq™ on a QuantStudio™ 5 system, with GAPDH as the endogenous control.

In vivo confocal microscopy evaluation of corneal endothelial safety

Male Sprague-Dawley rats (SD, 6 weeks old) were anesthetized with isoflurane and randomly assigned to three groups: (i) untreated control, (ii) ultrasound alone (US, 1.5 W/cm^2, 1 MHz, 5 min, applied to the closed eyelid via coupling gel), and (iii) MNs+BaTiO3@Au+US (microneedle insertion followed immediately by the same US protocol). Immediately after treatment, a topical drop of 0.5% proparacaine hydrochloride was instilled, and the cornea was examined using a Heidelberg Retinal Tomograph III Rostock Cornea Module (HRT3-RCM, Heidelberg Engineering, Heidelberg, Germany).

Establishment of keratitis model and evaluation in vivo

Male SD rats (6 weeks old) were obtained from Shenzhen University Model Animal Center. All the animal procedures were performed in compliance with the guidelines of the Institutional Animal Care and Use Committee of Shenzhen University Medical School. (Approval No. IACUC-202300142). After isoflurane anesthesia, corneas received topical 0.5% lidocaine hydrochloride. The corneal epithelium was then removed, followed by the addition of 20 μL S. aureus bacterial suspension (1×10^7 CFU/mL). 24 hours post-infection, the corneas of rats were treated with commercial eye drop group (tobramycin dexamethasone, abbreviated as Drop); MNs+US; MNs+BaTiO3+US; MNs+BaTiO3@Au+US, respectively, one time per day for 3 days. Each time, a coupling agent to the eyelid and sonicate for 5 min (1.5 W/cm^2, 1 MHz) for the US treatment. The untreated rats were used as control. Daily ophthalmic examinations included observation via a surgical microscope and sodium fluorescein staining (Days 1, 3, 5, and 7) to quantify epithelial defects.

On day 7 post-infection, the part of the rats were euthanized and the whole corneas were aseptically excised using ophthalmic scissors and forceps. Each cornea was placed in a sterile microcentrifuge tube containing 200 μL of sterile PBS and homogenized on ice using a sterile plastic pestle. The homogenate was serially diluted in sterile PBS, and 100 μL of each dilution was spread onto tryptic soy agar plates. Plates were incubated at 37 ° C for 20 h, and colony-forming units (CFU) were observed.

On day 7, the corneas from the rest rats were processed for HE and immunohistochemical staining. HE staining: deparaffinized sections underwent hematoxylin/eosin sequential staining. Immunohistochemistry staining: deparaffinized sections were incubated with IL-6 and TNF-α primary antibodies and HRP-conjugated secondaries, followed by staining with DAB and hematoxylin. Immunofluorescence analysis, deparaffinized sections were incubated with iNOS/CD 206, α-SMA, and ZO-1 primary antibodies and AlexaFluor-conjugated secondaries, followed by the mounting with DAPI solution. All slides were imaged using fluorescence microscopy (Leica, Germany).

Statistical analysis

All the results are presented as the means ± standard deviation. Statistical analysis was carried out using one-way ANOVA followed by post-hoc test to determine the degree of significance by the software of Prism 10. Statistical significance was defined as $^*p < 0.05$, $^{**}p < 0.01$, $^{***}p < 0.001$, $^{****}p < 0.0001$.

Supporting Figures

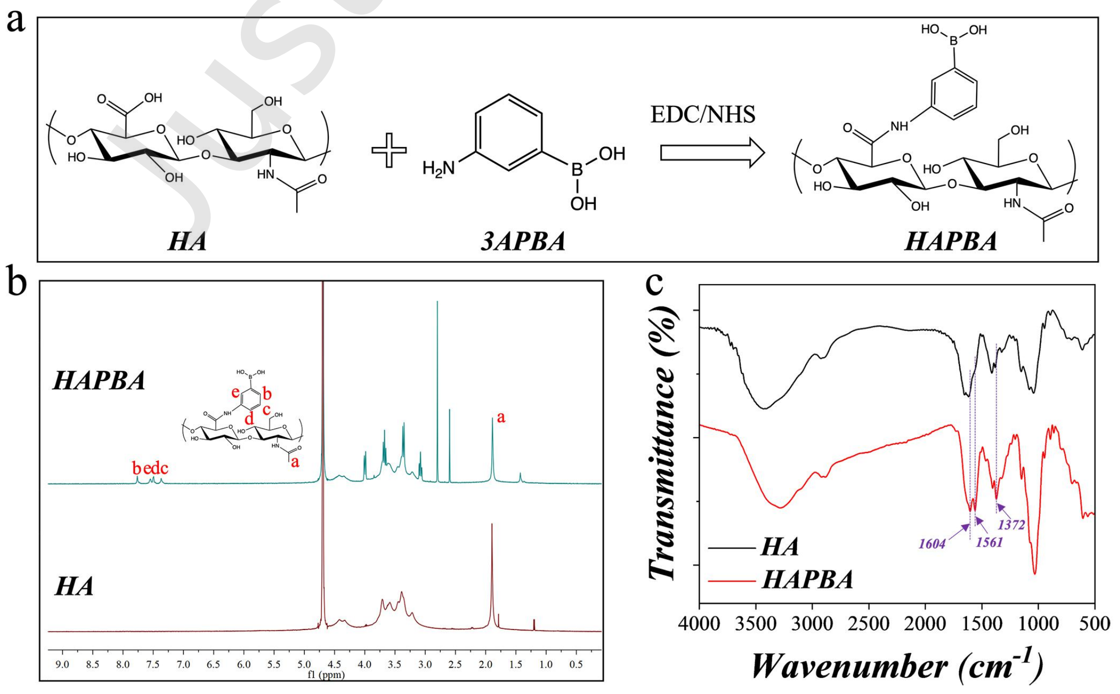

Figure S1. (a) Synthesis of HAPBA. ^{1}HNMR (b) and FTIR (c) of HA and HAPBA.

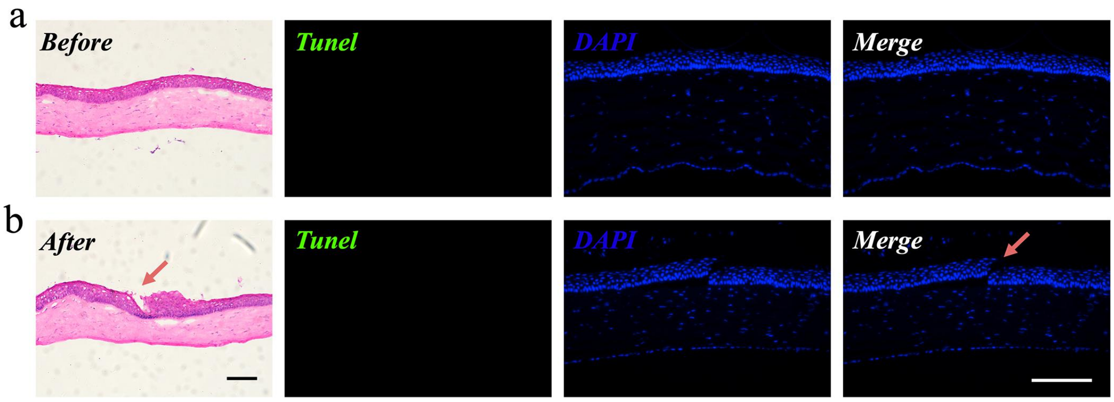

Figure S2. Representative HE and tunel/DAPI staining images of rat cornea before (a) and after (b) MNs insertion. Scale bars: 200 μm.

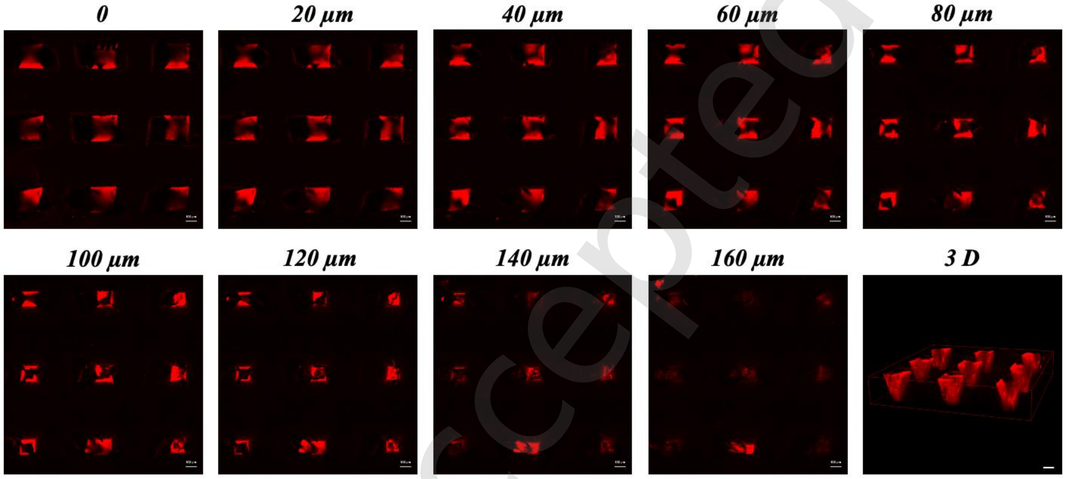

Figure S3. Representative confocal Z-stack images of a rat cornea immediately after insertion and removal of a rhodamine B-labeled core-shell microneedle. Scale bar: 100 μm.

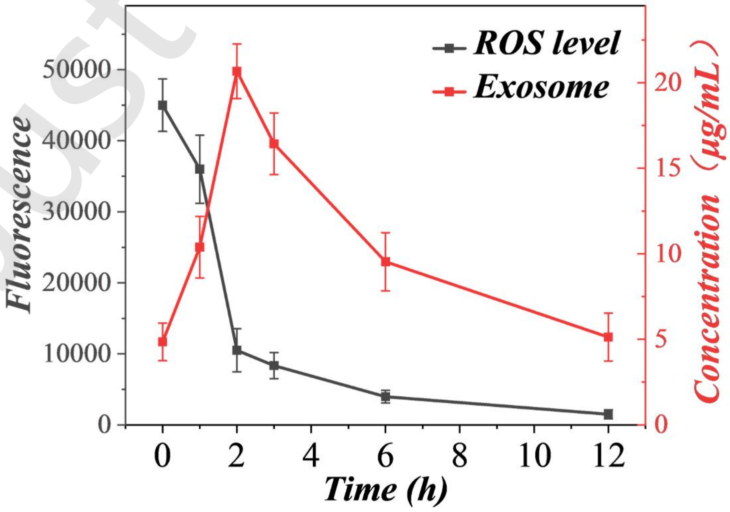

Figure S4. ROS level and exosome concentration in the bacteria infected cornea at different time points after treatment with MNs and US. n=3 independent measurements; data are shown as mean ± SD.

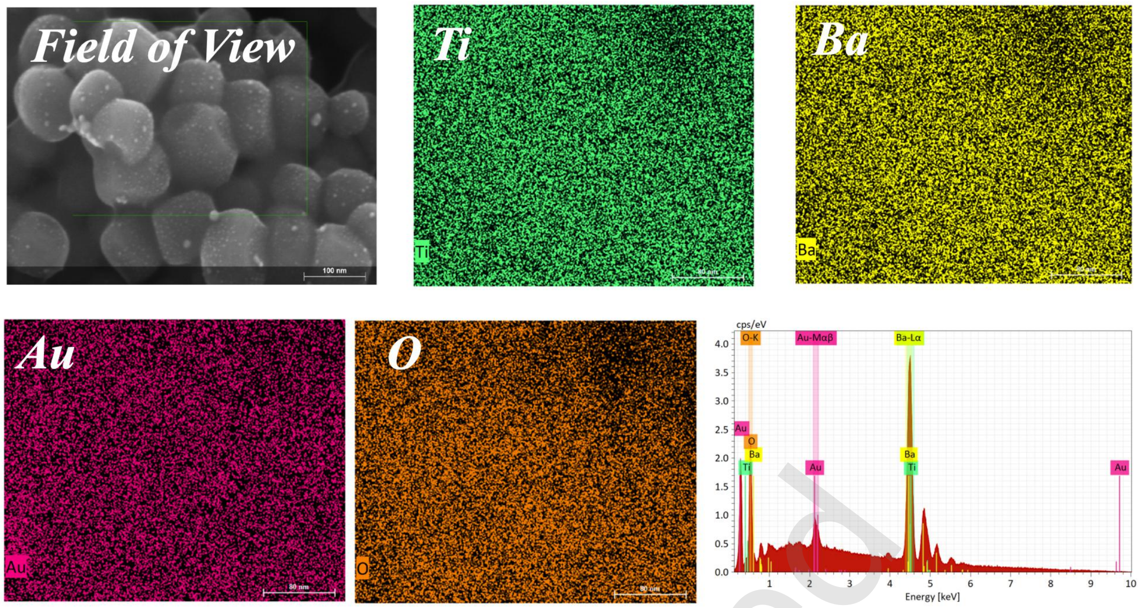

Figure S5. EDS mapping shows the element composition of $BaTiO_3$@Au NPs.

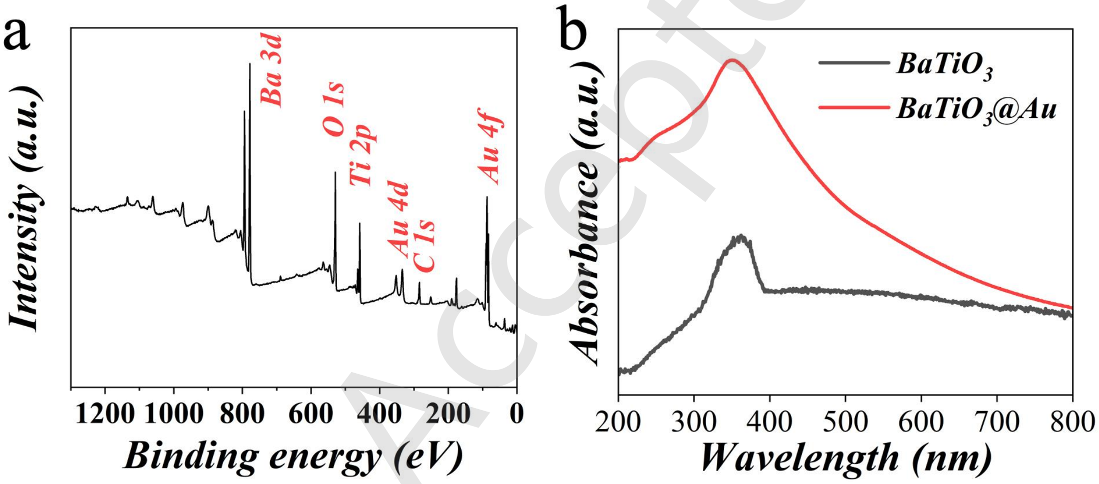

Figure S6. (a) XPS spectra of $BaTiO_3$@Au NPs. (b) UV-vis spectrum of $BaTiO_3$ and $BaTiO_3$@Au NPs.

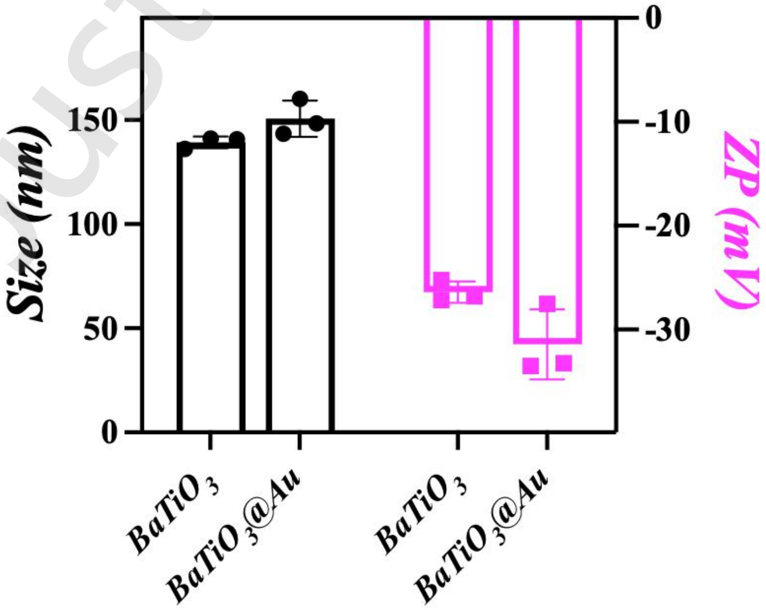

Figure S7. Size (a) and zeta potential (b) of $BaTiO_3$ and $BaTiO_3$@Au NPs. n=3 independent measurements; data are shown as mean ± SD.

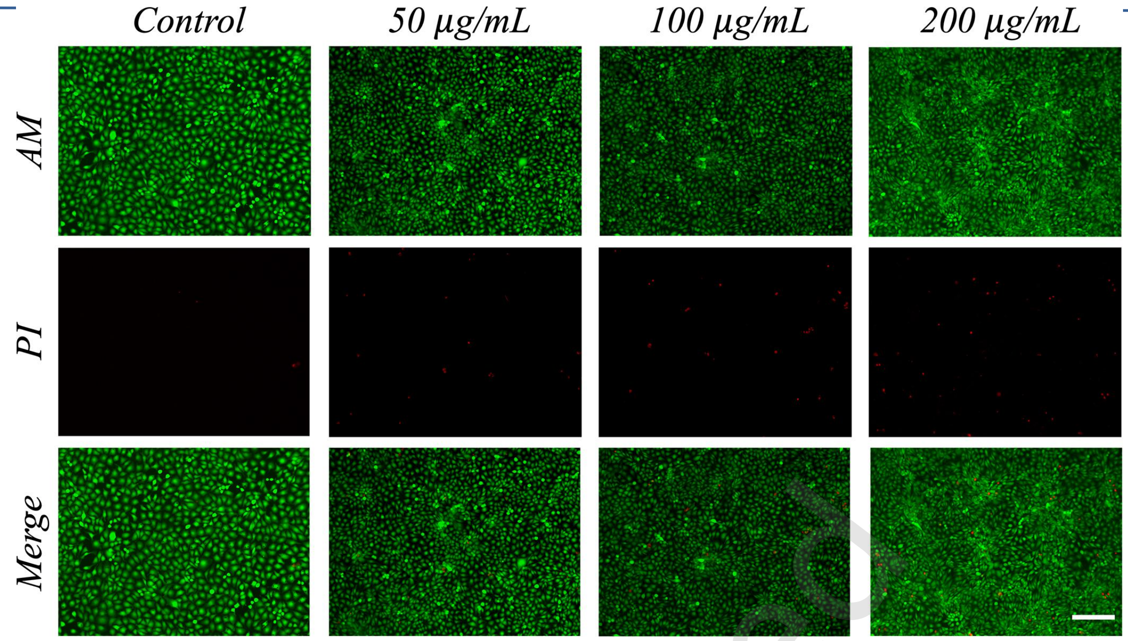

Figure S8. The Live/Dead staining images of HCECs after treatment with the microneedles at varied BaTiO3@Au concentrations for 3 days. Scale bar: 200 μm.

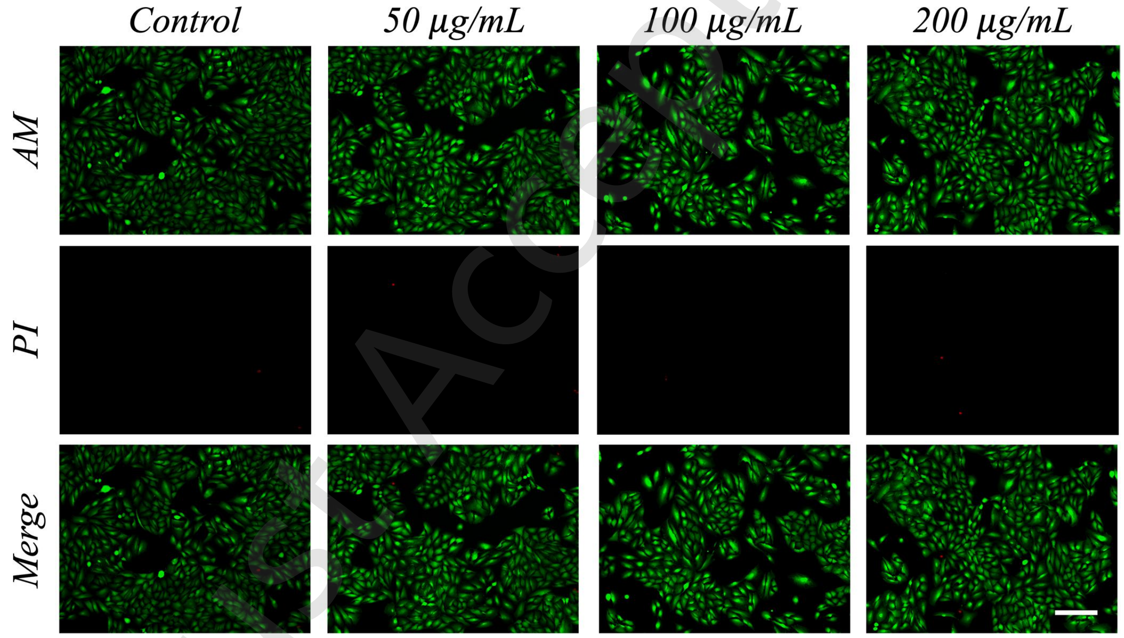

Figure S9. The Live/Dead staining images of HKs after treatment with the microneedles at varied $BaTiO_3$@Au concentrations for 3 days. Scale bar: 200 μm.

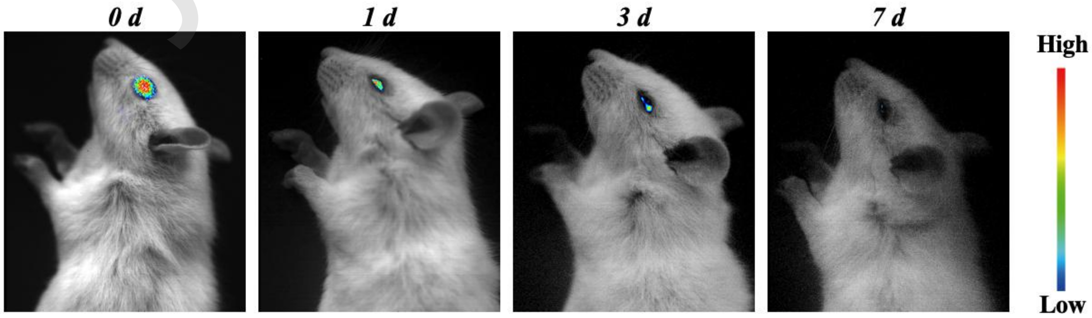

Figure S10. In vivo fluorescence imaging of Cy5.5-labeled BaTiO3@Au nanoparticles injected into the rat corneal stroma.

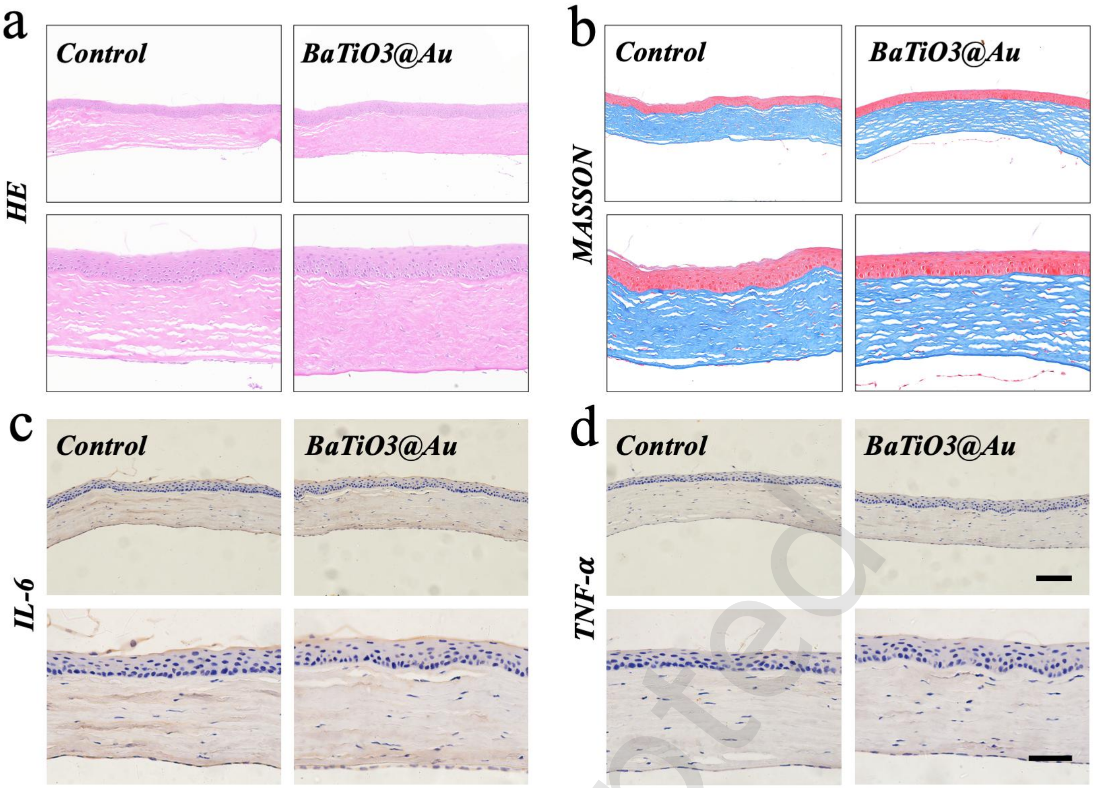

Figure S11. Histological and immunohistochemical assessment of corneas one month after intracorneal injection of BaTiO$_3$@Au nanoparticles compared to untreated normal controls. Scale bars: 100 μm, and 50 μm in the enlarged images.

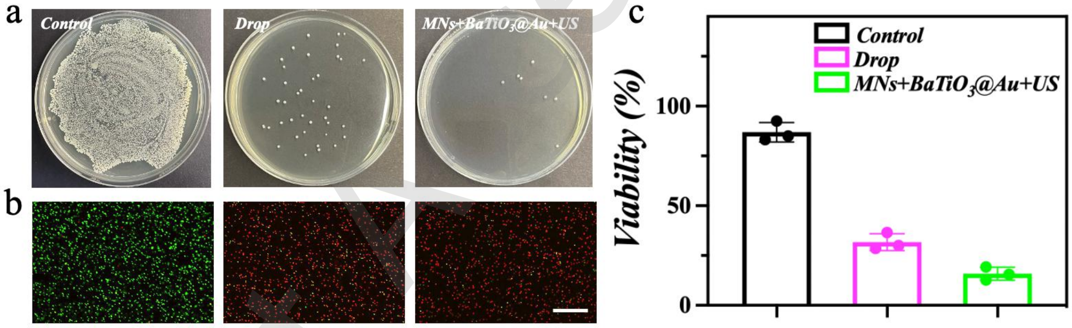

Figure S12. (a) Representative agar plate photographs showing MRSA colonies recovered after treatment with the indicated conditions. (b) Representative Live/Dead fluorescence images of MRSA under the corresponding treatments. (c) Quantitative analysis of bacterial survival viability. n=3 independent measurements; data are shown as mean ± SD.

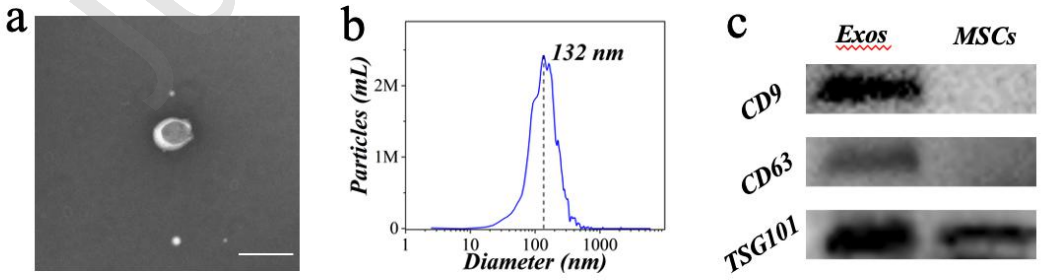

Figure S13. (a) Representative TEM image of exosome. (b) NTA measurement shows size distribution of exosome. (c) WB result shows the protein expression in exosomes and MSCs. Scale bar: 200 nm.

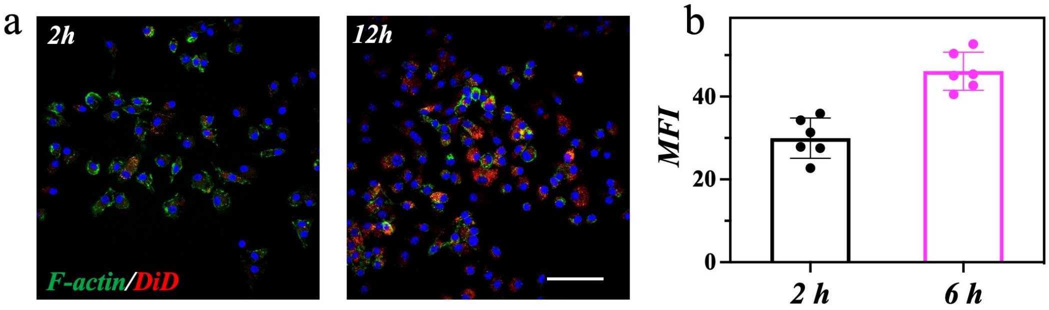

Figure S14. (a) Fluorescent images show the uptake of exosomes by HCECs under different time. HCECs were stained with phalloidin (green) and DAPI (blue). Exosomes were labeled with DiD (red). (b) Mean fluorescent intensity of DiD labeled exosomes in (a). n=6 independent measurements; data are shown as mean ± SD. Scale bar: 50 μm.

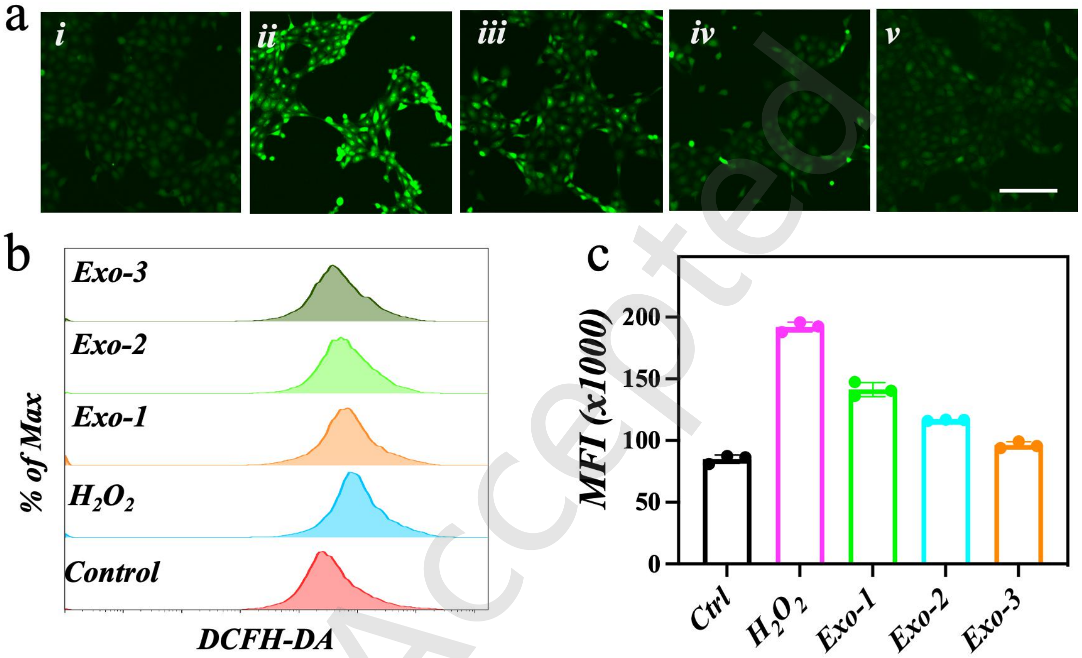

Figure S15. (a) DCFH-DA staining of HCECs under different treatment: i) control; ii) H2O2; iii) H_2O_2+exosomes-1; iv) H_2O_2+exosomes-2; v) H_2O_2+exosomes-3. Flow cytometry histogram (b) and mean fluorescence intensity (c) of DCFH-DA in HCECs. n=3 independent measurements; data are shown as mean ± SD. Scale bar: 100 μm.

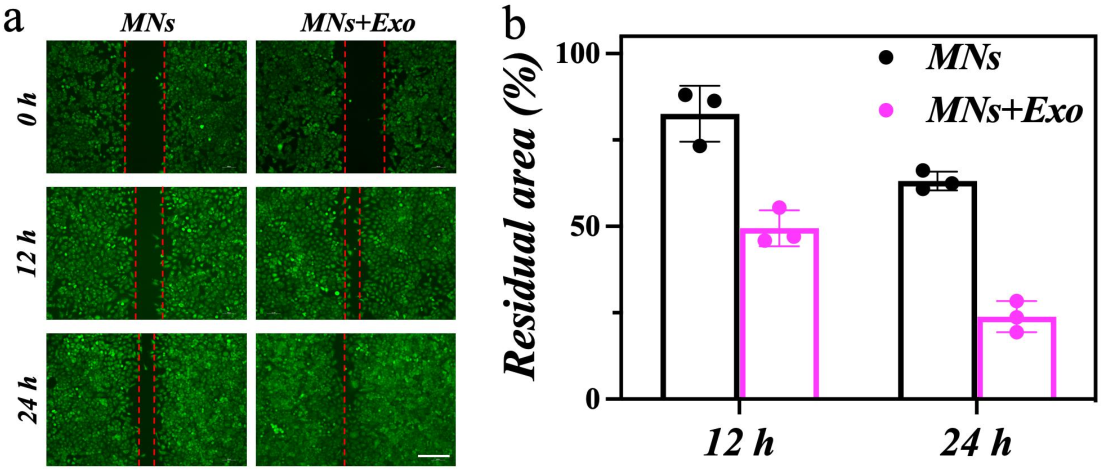

Figure S16. (a) Representative AM staining fluorescent images of HCECs show the migration of the cells under treatment with or without exosomes. (b) The quantitative analysis of wound healing assay with various treatments in HCECs. n=3 independent measurements; data are shown as mean ± SD. Scale bar: 200 μm.

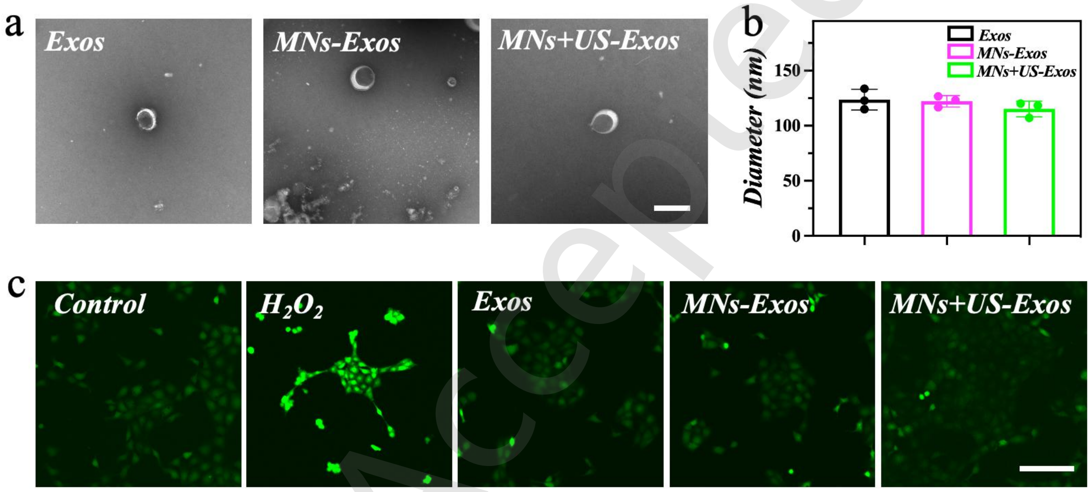

Figure S17. (a) Representative TEM images of exosomes from the three conditions. Scale bars: 200 nm. (b) Mean hydrodynamic diameters of exosomes in the three groups. No significant size alterations were observed (n=3 independent measurements; data are shown as mean ± SD). (c) DCFH‑ DA fluorescence images of HCECs showing intracellular ROS levels after the indicated treatments. Scale bars: 100 μm.

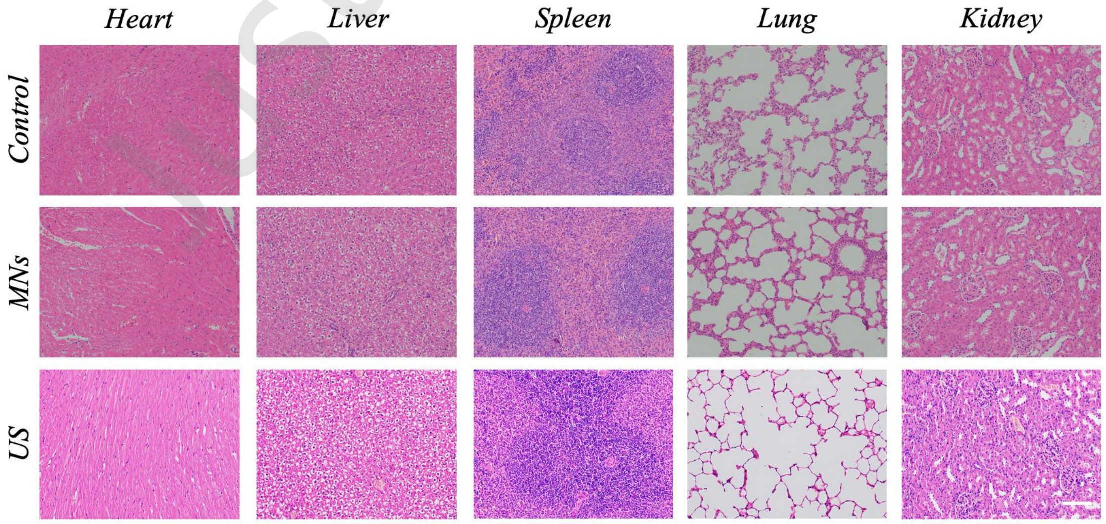

Figure S18. Representative HE staining images of heart, liver, spleen, lung, and kidney from normal rats (control), US only, and rats subcutaneously implanted with $BaTiO_3$@Au incorporated microneedle for 2 weeks, respectively. Scale bar: 100 μm.

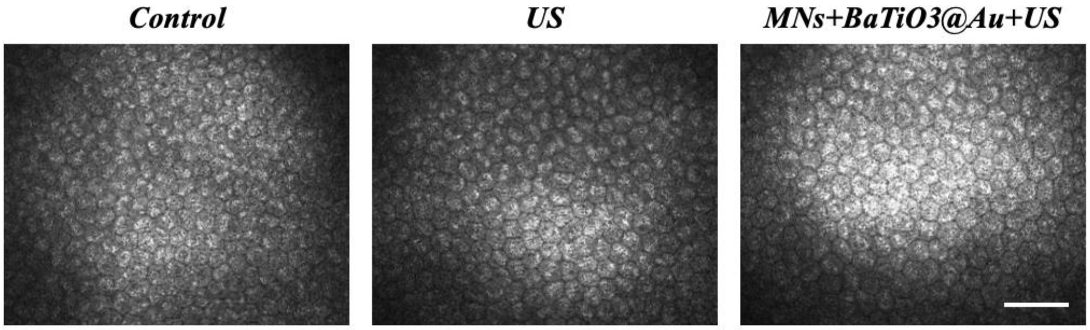

Figure S19. Representative images of the central corneal endothelium acquired immediately after different treatment, including untreated control, ultrasound alone, and MNs+$BaTiO_3$@Au+US. Scale bar: 50 μm.

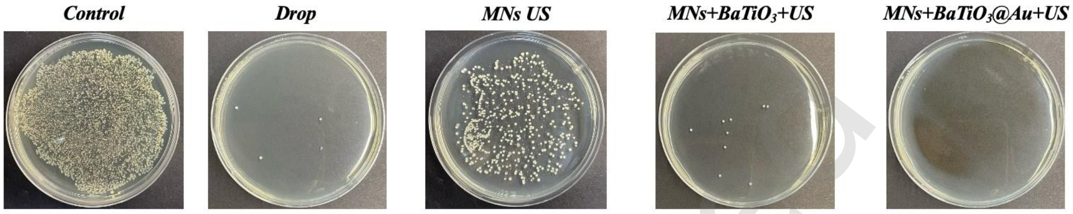

Figure S20. Representative agar plate photographs showing bacterial colonies recovered from infected rat corneas after 7 days of treatment.

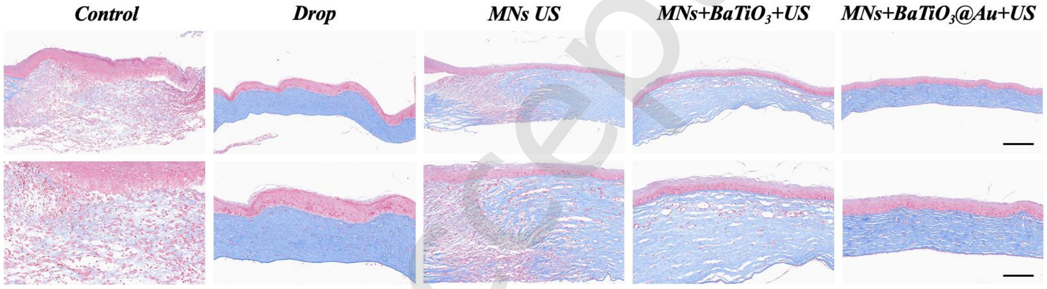

Figure S21. Representative collagen immunofluorescence staining images of infected cornea subjected to: untreated cornea (i), drop (ii), MNs+US (iii), MNs+$BaTiO_3$+US (iv), and MNs+$BaTiO_3$@Au+US (v). Scale bars: 200 μm, and 100 μm in the enlarged images.

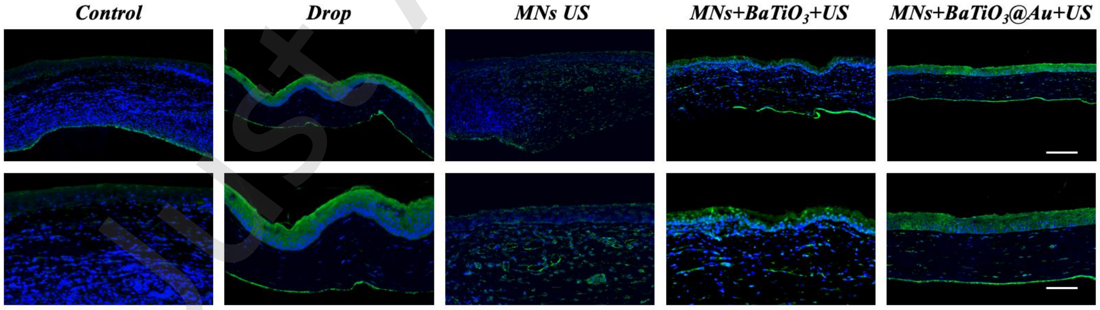

Figure S22. Representative ZO-1 immunofluorescence images of infected cornea subjected to: untreated cornea (i), drop (ii), MNs+US (iii), MNs+$BaTiO_3$+US (iv), and MNs+$BaTiO_3$@Au+US (v). Scale bars: 200 μm, and 100 μm in the enlarged images.

Table 1. qPCR primer sequences.

Gene	Sequence (5’-3’)
IL-1β	
Forward	GCAACTGTTCCTGAACTCAACT
Reverse	ATCTTTTGGGGTCCGTCAACT
IL-6	
Forward	CCGGAGAGGAGACTTCACAG
Reverse	TCCACGATTTCCCAGAGAAC
iNOS	
Forward	GTTCTCAGCCCAACAATACAAGA
Reverse	GTGGACGGGTCGATGTCAC
IL-10	
Forward	GCTCTTACTGACTGGCATGAG

Reverse	CGCAGCTCTAGGAGCATGTG
Arg-1	
Forward	CTCCAAGCCAAAGTCCTTAGAG
Reverse	AGGAGCTGTCATTAGGGACATC
CD 206	
Forward	CTCTGTTCAGCTATTGGACGC
Reverse	CGGAATTTCTGGGATTCAGCTTC

References

1. Lee, S. Y.; Hong, E. H.; Jeong, J. Y.; Cho, J.; Seo, J. H.; Ko, H. J.; Cho, H. J., Esterase-sensitive cleavable histone deacetylase inhibitor-coupled hyaluronic acid nanoparticles for boosting anticancer activities against lung adenocarcinoma. *Biomater. Sci.* **2019**, *7* (11), 4624-4635.

2. Li, M.; Shi, X.; Yang, B.; Qin, J.; Han, X.; Peng, W.; He, Y.; Mao, H.; Kong, D.; Gu, Z., Single-component hyaluronic acid hydrogel adhesive based on phenylboronic ester bonds for hemostasis and wound closure. *Carbohydr. Polym*. **2022**, *296*, 119953.

3. Xu, S.; Guo, L.; Sun, Q.; Wang, Z. L., Piezotronic Effect Enhanced Plasmonic Photocatalysis by AuNPs/BaTiO3 Heterostructures. *Adv. Funct. Mater*. **2019**, *29* (13), 1808737.

4. Liu, H.; Zhu, R.; Shi, N.; Zhang, L.; Li, S.; Zhang, J., Piezotronic Effect Induced Schottky Barrier Decrease to Boost the Plasmonic Charge Separation of BaTiO(3)-Au Heterojunction for the Photocatalytic Selective Oxidation of Aminobenzyl Alcohol. *ACS Appl. Mater. Interfaces* **2022**, *14* (50), 55548-55558.